Article

Biodegradable Janus sonozyme with continuous reactive oxygen species regulation for treating infected critical-sized bone defects

Zixuan Ou[1,2], Junyu Wei[1,2], Jie Lei[1,2], Di Wu[1,2], Bide Tong[1], Huaizhen Liang[1], Dingchao Zhu[1], Hongchuan Wang[1], Xingyu Zhou[1], Hanpeng Xu[1], Zhi Du[1], Yifan Du[1], Lei Tan ●[1] ✉, Cao Yang ●[1] ✉ & Xiaobo Feng ●[1] ✉

Critical-sized bone defects are usually accompanied by bacterial infection leading to inflammation and bone nonunion. However, existing biodegradable materials lack long-term therapeutical effect because of their gradual degradation. Here, a degradable material with continuous ROS modulation is proposed, defined as a sonozyme due to its functions as a sonosensitizer and a nanoenzyme. Before degradation, the sonozyme can exert an effective sonodynamic antimicrobial effect through the dual active sites of MnN_4 and Cu_2O_8. Furthermore, it can promote anti-inflammation by superoxide dismutase- and catalase-like activities. Following degradation, quercetin-metal chelation exhibits a sustaining antioxidant effect through ligand-metal charge transfer, while the released ions and quercetin also have great self-antimicrobial, osteogenic, and angiogenic effects. A rat model of infected cranial defects demonstrates the sonozyme can rapidly eliminate bacteria and promote bone regeneration. This work presents a promising approach to engineer biodegradable materials with long-time effects for infectious bone defects.

Critical-sized bone defects typically arise subsequent to trauma or tumors and are challenging to facilitate autologous healing due to the large size of the defect[1]. Furthermore, critical-sized bone defects frequently co-occur with infection by drug-resistant bacteria, which may result from bacterial invasion or improper handling[2,3]. Methicillin-resistant *Staphylococcus aureus* (MRSA) is the primary causative agent[4]. Failure to adequately treat these defects can result in chronic pain and even disability[5]. The prolonged presence of bacteria at the site of infection can induce osteoclasts and increase bone lysis by releasing harmful substances, such as *Staphylococcus aureus (S. aureus)* A protein, which can have a detrimental effect on bone repair[6]. Furthermore, bacteria can also release metabolites such as lipopolysaccharide (LPS) to activate cellular inflammatory pathways and inhibit

bone repair[7]. Consequently, the successful treatment of infectious bone defects necessitates the simultaneous addressing of both the bacterial infection and the inflammatory micro-environment. Currently, antibiotics and surgery are the most commonly employed treatments[8]. Although these two methods can inhibit bacterial infection, they are not effective in improving the inflammation of the infected lesion. In addition, the abuse of antibiotics can lead to the development of antibiotic resistance, while surgical treatment may also have the unintended consequence of exacerbating the severity of the bone defect[9]. In conclusion, it is of paramount importance to develop a therapeutic approach that can effectively eliminate bacterial infections while simultaneously suppressing the local inflammatory micro-environment.

[1]Orthopaedic Department, Union Hospital, Tongji Medical College, Huazhong University of Science and Technology, Wuhan, PR China. [2]These authors contributed equally: Zixuan Ou, Junyu Wei, Jie Lei, Di Wu. ✉e-mail: tanlei_union@hust.edu.cn; caoyangunion@hust.edu.cn; fengxiaobo@hust.edu.cn

Sonodynamic therapy (SDT) has emerged as a promising non-invasive and efficacious strategy for bacterial clearance[10]. The fundamental mechanism underlying bactericidal activity is the generation of reactive oxygen species (ROS) through the reaction with water and oxygen, facilitated by the transfer of electrons in the presence of ultrasound (US) and sonosensitizer[11]. ROS can eliminate bacteria by a variety of mechanisms, including disruption of the electron transport chain, resulting in the death of pathogenic bacteria due to oxidative stress and impaired energy metabolism[12]. It is, however, important to note that although ROS are effective in eliminating bacteria, they can also have adverse effects on normal cells and tissues surrounding the infection. ROS can contribute to the progression of local inflammation by promoting macrophage M1 polarisation[13]. Moreover, ROS can also induce mitochondrial dysfunction in stem cells, thereby inhibiting their osteogenic differentiation[12]. In conclusion, ROS can be considered a double-edged sword. Nanoenzymes, which are catalytic nanomaterials with enzyme-like properties, can mimic the structure of natural antioxidant enzymes to play the role of superoxide dismutase (SOD) and catalase (CAT) activities, thereby catalyzing the generation of water and oxygen from ROS[14]. The use of nanoenzymes is pervasive due to their cost-effectiveness, stability, tunable catalytic activity, and ease of mass production[15]. Nevertheless, the development of materials that are capable of both generating and removing ROS represents a challenge in the treatment of infected bone defects. Additionally, the selection of biocompatible materials is of paramount importance for the treatment of infected bone defects, as materials that are difficult to biodegrade can impede bone tissue healing and exacerbate inflammation.

Currently, a plethora of biocompatible materials are available in treating infectious bone defects. Organic sonosensitizers, such as porphyrin and its derivatives, 5-aminolevulinic acid and phthalocyanine, which have high SDT efficiency and rapid degradation, are widely used[16–18]. Furthermore, degradable nanoenzymes, such as MnPcBc, Prussian blue and phosphate-based glass (PBG), have been employed in antioxidant studies[14,19–21]. However, while good biocompatibility is beneficial in preventing tissue damage and local inflammation caused by material implantation, it is of significant challenge for materials with excellent degradation properties to exert a long-term effect. As the sonosensitizers or nanoenzymes rely on the intrinsic properties of the material to function, the SDT or antioxidant effect is diminished when the material undergoes degradation, which can be disadvantageous for long-term treatment. Drug loading represents an improved method of maintaining functionality following material degradation. However, the drug itself may still be metabolised by cells, resulting in a loss of its effect[22]. Consequently, the development of biomaterials with optimal biocompatibility and long-time efficacy represents a pivotal aspect of the management of infectious bone defects.

In light of the aforementioned considerations, we have developed a degradable material with a long-time effect. It is both a sonosensitizer and a nanoenzyme, so we define it as a sonozyme. This sonozyme can induce oxidative stress through SDT for precise eradication of bacterial invasion and exert antioxidant capacity by adsorbing ROS for bone repair. Given its capacity to both remove and generate ROS, we conclude that it is a Janus material. As illustrated in Fig. 1, it is a two-dimensional metal organic nanosheet composed of copper and manganese, meanwhile coordinating with quercetin (que) (MON(CuMn)-Q). MON(CuMn)-Q is capable of generating a substantial quantity of $^1O_2$ under US, which is effective in eliminating MRSA infections. Furthermore, it has the capacity to adsorb ROS, thereby combating inflammation through the dual active sites of MnN_4 and Cu_2O_8, before undergoing degradation. Following degradation, MON(CuMn)-Q continues to demonstrate effective antimicrobial and antioxidant properties through the release of copper, manganese and que. Copper, manganese ions and que have been demonstrated to possess antimicrobial properties, and the controlled release of ions and que can effectively inhibit bacterial growth[22–24]. Furthermore, que can be complexed with copper

and manganese to form ligand-metal charge transfer (LMCT), which enhances the antioxidant capacity of que by modifying the valence of the metal ions. Finally, copper, manganese ions and que also possess osteogenic and angiogenic activities, which facilitate the rapid repair of bone tissue. In a rat cranial bone defect model infected with MRSA, we successfully achieved antibacterial and anti-inflammatory treatment by encapsulating MON(CuMn)-Q in an antibacterial hydrogel (MON(CuMn)-Q-J). In conclusion, we have constructed a degradable material with continuous ROS regulation and it has been successfully demonstrated to promote the repair of infected cranial bone defects.

Results

Structural characterization

MON(Cu) and MON(CuMn) were synthesised from TCPP and MnTCPP, respectively, with $Cu(NO_3)_2$ in support of trifluoroacetic acid. MON(CuMn)-Q was further enriched with que on the basis of MON(CuMn). The molecular structures of MON(Cu) and MON(CuMn) were illustrated in Figs. 2a, d. Since the bimetallic MOF was synthesised from MnTCPP, manganese could coordinate with four N atoms, which represented the central porphyrin linker. During the self-assembly process, copper would combine with the carboxyl group of MnTCPP to form the structure of Cu_2O_8[25]. The successful fabrication of MON(Cu) and MON(CuMn) was further confirmed by scanning electron microscopy (SEM) and transmission electron microscopy (TEM), which revealed the ultrathin sheet-like morphology of the structures (Supplementary Figs. 1 and 2). The size of MON(Cu) and MON(CuMn) was approximately 1–2 μm and 2–3 μm, respectively. Then, the prepared MON(Cu) and MON(CuMn) were separately disassembled into smaller nanosheets by the mechanical force of probe sonication before biological experiments. It can be concluded that the nanosheet size can be smaller than 200 nm after probe sonication, suggesting that the nanosheet size can be adjusted (Figs. 2b, e). The average thickness of MON(Cu) was determined to be approximately 2.9 nm by atomic force microscopy (AFM) (Fig. 2c). MON(CuMn) exhibited a thickness comparable to that of MON(Cu), which was approximately 2.7 nm (Fig. 2f). X-ray diffraction (XRD) was employed to characterize the crystalline structure of MON(Cu), MON(CuMn), MON(CuMn)-Q (Supplementary Fig. 3). Three distinct peaks, indexed as (110), (002) and (004), were ascribed to the tetragonal structure[26,27]. The (002) peak is often correlated with nanosheet structures[28], while the broad (004) peak suggests an ultrathin crystal feature[29]. To further analyze the elemental composition, the energy dispersive spectrum (EDS) was employed and the result demonstrated that Cu, Mn, N, C, and O were uniformly distributed over the MON(CuMn) and MON(CuMn)-Q (Fig. 2g, Supplementary Figs. 4 and 5). This preliminary evidence suggested that Cu and Mn atoms were homogeneously doped into MON(CuMn) and MON(CuMn)-Q.

The X-ray photoelectron spectroscopy (XPS) survey further indicated the element composition of the nanosheets (Fig. 2h). From Fig. 2i, it could be concluded that the elemental content of MON(Mn) involved Mn 2p (0.81%), O 1s (14.28%), N 1s (4.87%) and C 1s (80.04%). The elemental content of MON(Cu) was found to comprise Cu 2p (3.07%), O 1s (11.81%), N 1s (6.1%) and C 1s (79.02%). Doped with manganese ions, the elemental content of MON(CuMn) was found to include Cu 2p (1.60%), Mn 2p (1.18%), O 1s (12.46%), N 1s (6.56%) and C 1s (78.20%). The final product, MON(CuMn)-Q, exhibited the following elemental composition: Cu 2p (1.29%), Mn 2p (1.10%), O 1s (13.61%), N 1s (6.73%) and C 1s (77.27%). In conclusion, the aforementioned results demonstrated the successful synthesis of the nanosheets. To further investigate the effect of different copper and manganese contents and the loading of que on the nanosheets, the elemental peaks were further used for comparison. In Fig. 2j, the N 1s region of MON(Mn) and MON(Cu) contained metal-N (402.51 and 401.45 eV), C = N (400.16 and 400.02 eV) and C-N (398.88 and 398.88 eV) which was consistent with previous studies[24,30]. The
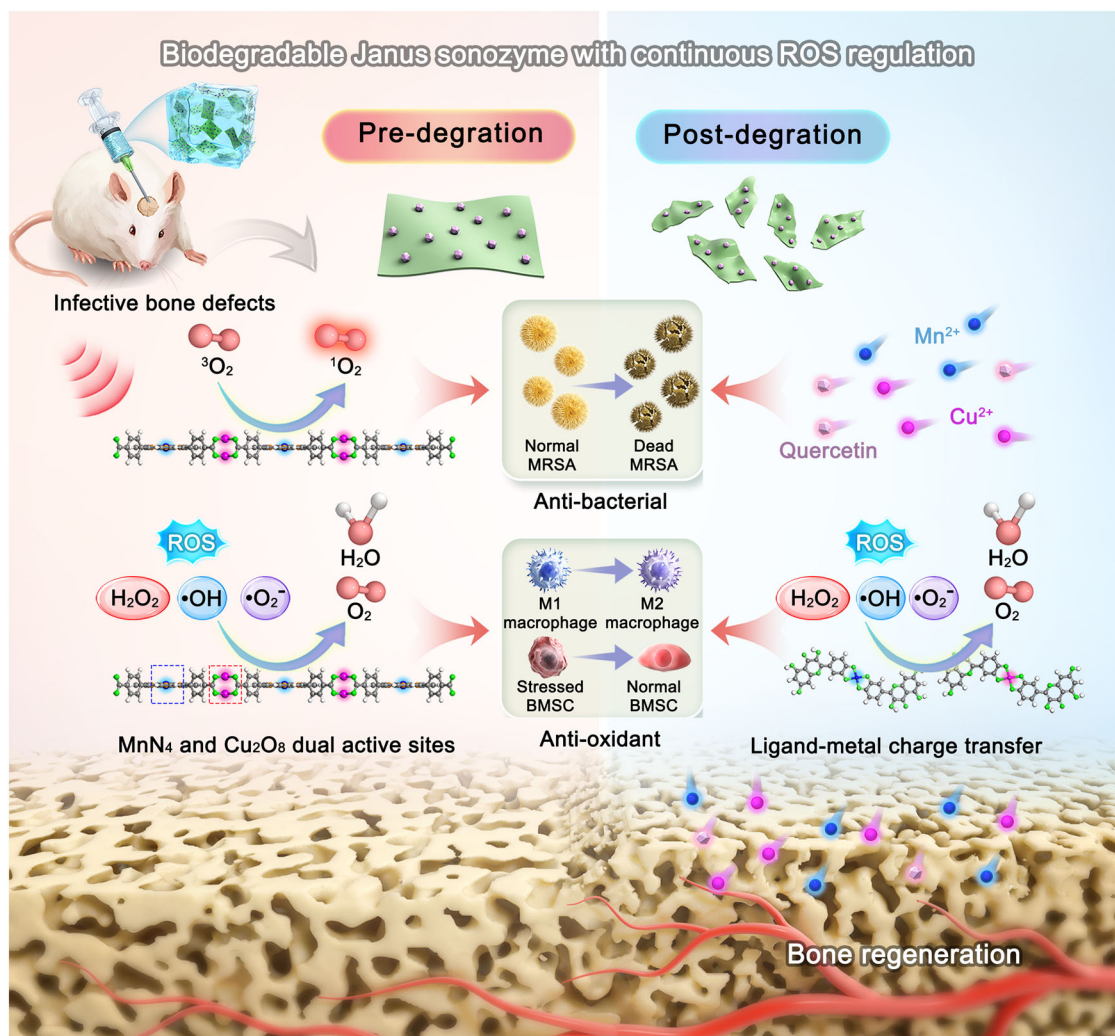
Fig. 1 | Schematic representation of the mechanism via which the Janus sonozyme treats infected critical-sized bone defects. Before degradation, the sonozyme can exert an effective sonodynamic antimicrobial effect through the dual active sites of MnN_4 and Cu_2O_8. Furthermore, it can promote anti-inflammation by superoxide dismutase- and catalase-like activities. Following degradation, quercetin-metal chelation exhibits a sustaining antioxidant effect through ligand-metal charge transfer, while the released ions and quercetin also have great self-antimicrobial, osteogenic, and angiogenic effects.

binding energies of the sub-peaks of the N 1s region in MON(Mn) and MON(Cu) were similar, which indicated the chemical environment of the N atoms in MON (Mn) and MON (Cu) was almost the same. When doped with manganese in MON(Cu), C–N could not be observed by XPS, suggesting that the addition of manganese disrupted the original chemical environment and facilitated the breaking of the C-N bond. In addition, the loading of que resulted in minor shifts in the metal-N from 401.82 eV to 400.89 eV and in the C=N from 399.78 eV to 400.13 eV. Meanwhile, in Supplementary Fig. 6a, the C 1s peaks of MON(Mn), MON(Cu), MON(CuMn) and MON(CuMn)-Q were calibrated to 284.82 eV and could be fitted to four sub-peaks including C = N/C = O (284.80, 284.40, 284.80 and 284.80 eV), C-N/C-O (286.78, 285.93, 284.80 and 286.08 eV), C–C/C–H (289.32, 288.24, 287.15 and 287.35 eV) and C=C (291.99, 291.05, 289.52 and 289.22 eV). In Supplementary Fig. 6b, the O 1s region of the MON(Mn), MON(Cu), MON(CuMn) and MON(CuMn)-Q contained C-O (531.63, 531.79, 531.67 and 531.56 eV) and C = O (533.15, 532.39, 532.80 and 532.72 eV). In the Cu 2p spectra (Fig. 2k), two typical peaks at ~954 eV and ~932 eV ascribed to $Cu^+ 2p_{1/2}$ and $Cu^+ 2p_{3/2}$, and $Cu^{2+} 2p_{3/2}$ further confirmed the construction of the metal-organic frame (MOF), and the typical peak is around 935 eV[26]. The addition of que resulted in a decrease in $Cu^{2+} 2p_{1/2}$, $Cu^{2+} 2p_{3/2}$ and $Cu^+ 2p_{2/3}$ binding energy

in MON(CuMn), from 953.98 eV to 953.59 eV, 934.74 eV to 934.57 eV and 932.63 eV to 932.49 eV, respectively. This might be attributed to the fact that que might result in an augmented electron cloud around Cu^+ and Cu^{2+}, thereby reinforcing the shielding effect and reducing the binding energies. Finally, the peaks of $Mn^{2+} 2p_{1/2}$, $Mn^{4+} 2p_{3/2}$ and $Mn^{2+} 2p_{3/2}$ were observed in Fig. 2l. Doping with copper ions led to a decrease in $Mn^{2+} 2p_{1/2}$ from 654.73 eV to 652.66 eV, an increase in $Mn^{4+} 2p_{3/2}$ from 644 eV to 646.47 eV and an increase in $Mn^{2+} 2p_{3/2}$ from 642.51 eV to 642.78 eV. Que loading promoted a increase in $Mn^{2+} 2p_{1/2}$ binding energy (0.34 eV) and an decrease in $Mn^{4+} 2p_{3/2}$ (−1 eV) and $Mn^{2+} 2p_{3/2}$ binding energy (−0.27 eV), which might be attributed to the chelate of Mn^{4+} and Mn^{2+} with que. In conclusion, the above results demonstrated the successful preparation of the nanosheets. Furthermore, the doping of Mn and que had resulted in a change in the original chemical environment compared to MON(Cu).

Antioxidant performance and mechanism of nanosheet before degradation

The accumulation of ROS can promote cellular damage and thus inhibit bone tissue repair[31]. It is of great importance to scavenge excessive ROS in treating infective bone defects.
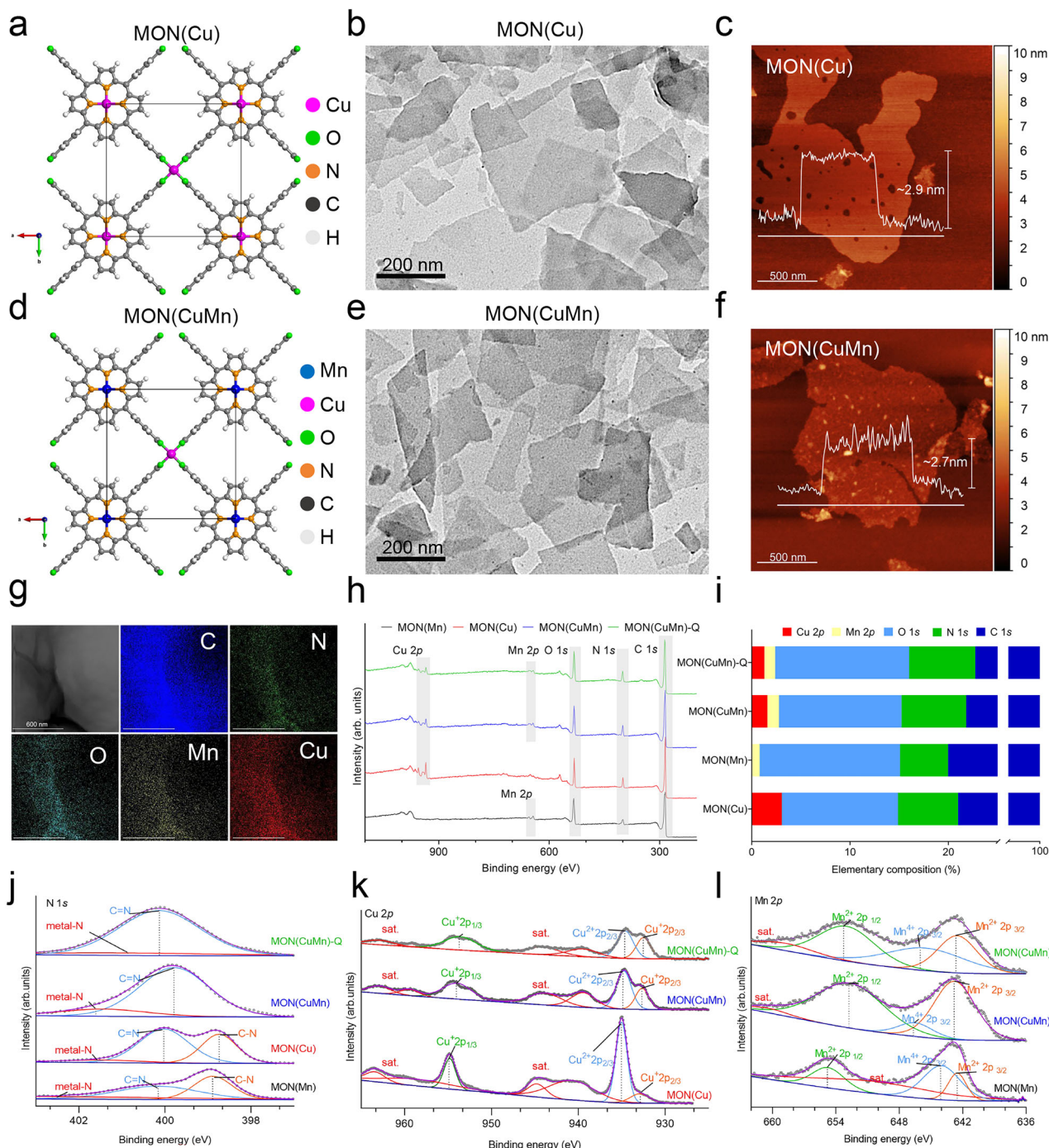
Fig. 2 | Structural characterization of the nanosheets. a The optimized structure for MON(Cu). **b** TEM images for MON(Cu) after probe sonication, scale bar: 200 nm, three independent experiments were repeated. **c** AFM image and corresponding height profiles of MON(Cu), scale bar: 500 nm, three independent experiments were repeated. **d** The optimized structure for MON(CuMn). **e** TEM image for MON(CuMn) after probe sonication, scale bar: 200 nm, three independent experiments were repeated. **f** AFM image and corresponding height profiles of MON(CuMn), scale bar: 500 nm, three independent experiments were repeated. **g** EDS mapping for MON(CuMn), scale bar: 600 nm, three independent experiments were repeated. **h** The total XPS spectra for MON(Mn), MON(Cu), MON(CuMn) and MON(CuMn)-Q. arb.units, arbitrary units. **i** The corresponding elementary composition of different nanosheets. XPS spectra for (**j**) N 1s, (**k**) Cu 2p and (**l**) Mn 2p. arb. units, arbitrary units; sat., satellite.

Cascade reactions involving several enzymes are required to maintain intracellular redox balance. SOD and CAT are common cascade reactions for scavenging ROS[32]. SOD is responsible for scavenging $\cdot O_2^-$ to H_2O_2 and O_2, while CAT further converts H_2O_2 to H_2O and O_2[31]. To investigate the SOD-like ability of the nanosheets further, an SOD activity kit was employed, and the results demonstrated that MON(CuMn)-Q exhibited the most pronounced $\cdot O_2^-$ scavenging ability (Fig. 3a). In Fig. 3b, CAT activity kit was employed to

investigate the H_2O_2 scavenging capacity of the nanosheets. The results indicated that MON(CuMn)-Q and MON(CuMn) exhibited a more robust H_2O_2 scavenging capacity than MON(Cu). Furthermore, the SOD- and CAT-like activities of the nanosheets were measured at varying pH levels. As illustrated in Supplementary Fig. 7, acidity exerts a decrease on nanosheet SOD-like activity, whereas nanosheets exhibit the highest CAT-like activity at neutral pH. It has been demonstrated that $\cdot OH$ is the most destructive ROS[33]. To further investigate the
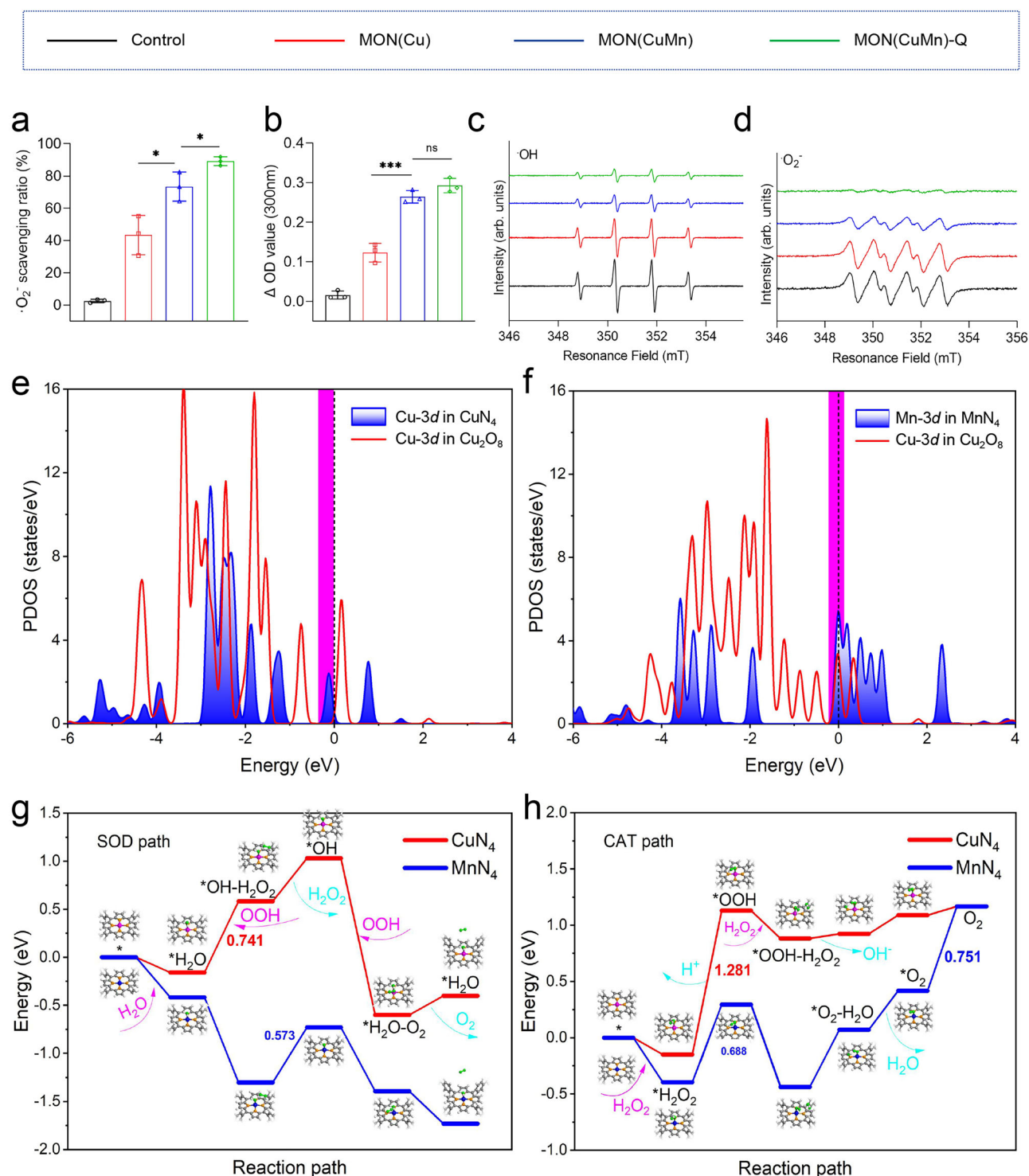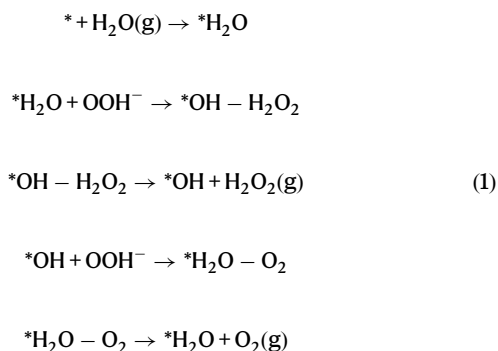
Fig. 3 | Antioxidation performance and mechanism of nanosheets before degradation. a The $\cdot O_2^-$ scavenging ratio of MON(Cu), MON(CuMn) and MON(CuMn)-Q ($p = 0.0269$; $p = 0.0446$), $n = 3$ independent experiments per group, data are expressed as mean $\pm$ SD, *$p < 0.05$, two-tailed ANOVA. **b** the CAT-like activity of MON(Cu), MON(CuMn), and MON(CuMn)-Q ($p = 0.0009$; $p = 0.1105$), $n = 3$ independent experiments per group, data are expressed as mean $\pm$ SD, ***$p < 0.001$, ns not significant, two-tailed ANOVA. ESR spectra of (**c**) the Fenton reaction and (**d**) the XO + X reaction system for different nanosheets. arb.units, arbitrary units. **e**, **f** The PDOS of MON(Cu) and MON(CuMn). PDOS, partial density of state. The theoretical calculation for (**g**) SOD and (**h**) CAT path of CuN$_4$ and MnN$_4$.
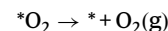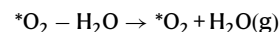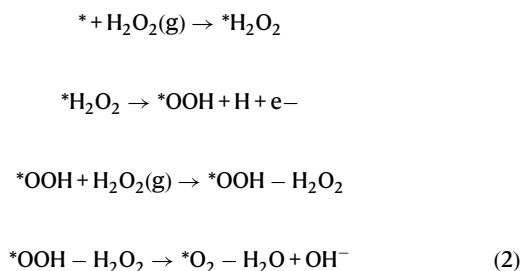
ability of nanosheets to scavenge $\cdot OH$, electron spin resonance (ESR) was employed. Following the addition of nanosheets to a Fenton reaction system, the result demonstrated a gradual weakening of the characteristic signal of $\cdot OH$ (1:2:2:1) (Fig. 3c). The order of the nanosheets in terms of their ability to scavenge $\cdot OH$ was as follows: MON(CuMn)-Q > MON(CuMn) > MON(Cu). In Fig. 3d, ESR

demonstrated that following the addition of nanosheets to a xanthine oxidase (XO) and xanthine (X) reaction system, the characteristic signal of $\cdot O_2^-$ (2:2:1:2:1:2) was diminished, indicating that MON(CuMn)-Q was capable of effectively scavenging $\cdot O_2^-$. This result aligned with the findings of Fig. 3a. Given that que has been demonstrated to possess antioxidant properties[22], it can be postulated that the loading of que

may have resulted in an enhanced adsorption of ROS by MON(Mn). Nevertheless, the underlying mechanism by which MON(CuMn) exhibits a higher oxidative capacity than MON(Cu) remains elusive. In order to explore the mechanism underlying the enhanced antioxidant activity of MON(CuMn), spin-polarized first-principles theoretical calculations were conducted based on density functional theory (DFT). The structural difference between MON(Cu) and MON(CuMn) could be attributed to the replacement of Cu by Mn in MON(CuMn), which resulted in the formation of the MnN_4 structure. Furthermore, the metal node of the MOF is the common active site in catalysis[27]. It can be postulated that the observed difference in catalytic performance between MON(Cu) and MON(CuMn) may be attributed to the differential catalytic activity of the MnN_4 and CuN_4 sites. The partial density of state (PDOS) analysis in Figs. 3e, f indicated that compared with CuN_4 site, dense peaks or even fusion peaks of the Mn-$3d$ orbit surrounding the Fermi level were detected at the MnN_4 site. The Mn-$3d$ orbitals are wider than the Cu-$3d$ orbitals, which have more unpaired electrons and, therefore, are more favourable for bonding. Consequently, it can be postulated that MnN_4 exhibits a greater capacity to adsorb ROS in comparison to CuN_4. In order to further verify our hypothesis, the catalytic pathways of SOD-like and CAT-like processes on the CuN_4 site of MON(Cu) and the MnN_4 site of MON(CuMn) were calculated. With regard to the SOD-like pathway at the CuN_4 and MnN_4 sites, it could be observed that H_2O was initially absorbed on CuN_4 or MnN_4, thereby forming $*H_2O$. Subsequently, a proton from the $*H_2O$ was captured by the OOH, resulting in the formation of H_2O_2. Subsequently, the $*OH$ oxidised the remaining OOH^- to O_2, thereby initiating the next catalytic cycle. The SOD reaction pathway could be described as follows:

$$* + H_2O(g) \rightarrow *H_2O$$

$$*H_2O + OOH^- \rightarrow *OH - H_2O_2$$

$$*OH - H_2O_2 \rightarrow *OH + H_2O_2(g) \qquad (1)$$

$$*OH + OOH^- \rightarrow *H_2O - O_2$$

$$*H_2O - O_2 \rightarrow *H_2O + O_2(g)$$

It has been reported that the highest energy barrier on the energy barrier diagram is the rate-determining step (RDS) in a continuous reaction process[14]. As illustrated in Fig. 3g and Supplementary Table 1, the RDS energy of MnN_4 was 0.573 eV, while the RDS energy of CuN_4 was 0.741 eV, indicating that the MnN_4 site was more prone to the SOD reaction than the CuN_4 site. For CAT-like pathway at the MnN_4 and CuN_4 sites, the H_2O_2 was first absorbed, and then an H^+ was lost. After another H_2O_2 reacted with the $*OOH$ left on the active site, $*OOH·H_2O_2$ intermediate formed, and eventually transformed into O_2. The CAT pathway could be concluded as follows:

$$* + H_2O_2(g) \rightarrow *H_2O_2$$

$$*H_2O_2 \rightarrow *OOH + H + e-$$

$$*OOH + H_2O_2(g) \rightarrow *OOH - H_2O_2$$

$$*OOH - H_2O_2 \rightarrow *O_2 - H_2O + OH^- \qquad (2)$$

$$*O_2 - H_2O \rightarrow *O_2 + H_2O(g)$$

$$*O_2 \rightarrow * + O_2(g)$$

The RDS energy of MnN_4 in the CAT pathway was 0.688 eV, which was less than the RDS energy of CuN_4, which was 1.281 eV (Fig. 3h and Supplementary Table 2). To further illustrate the mechanism of the efficient ROS scavenging of MnN_4 of MON(CuMn), the adsorption energies (E_{ads}) and bader charges (ΔQ) were calculated. Subsequently, the $*O_2$ and $*OH$ species were selected as they were pivotal intermediates in SOD-like and CAT-like pathways. The E_{ads} of MnN_4 and CuN_4 was calculated using the following equation:

$$\Delta E_{ads} = E(total) - E(surface) - E(*O_2)/E(*OH) \qquad (3)$$

In which E(total), E(surface), $E(*O_2)/E(*OH)$ represent the energy of $*O_2$ or $*OH$ absorbed on CuN_4 site of MON(Cu) and MnN_4 site of MON(CuMn), energy of the surface and energy of the free $*O_2$ or $*OH$ molecule, respectively. As indicated in Supplementary Table 3, the calculated E_{ads} of $*O_2$ or $*OH$ on MnN_4 (−0.75068825 eV and −2.91875543 eV) was found to be much smaller than CuN_4 (−0.07766123 and −1.15753080 eV), suggesting that the MnN_4 site was more favorable for the adsorption of $*O_2$ and $*OH$. ΔQ was further calculated and the result exhibited a comparable trend with E_{ads}. In Supplementary Table 4, the ΔQ of $*O_2$ and $*OH$ on CuN_4 is 0.0844 and 0.4609 eV respectively, which is smaller than ΔQ of $*O_2$ and $*OH$ on MnN_4 (0.4730 and 0.5778 eV). This indicated that MnN_4 was more conducive to electron transfer. The above results demonstrated that MnN_4 exhibited a greater capacity to adsorb ROS and transfer electrons than CuN_4. This explained why MON(CuMn)-Q and MON(CuMn) exhibited stronger antioxidant effects than MON(Cu).

Antioxidant performance and mechanism of nanosheet after degradation

It has been demonstrated that numerous materials rely on active sites to exert their antioxidant capacity[26]. However, the capacity of the materials to adsorb ROS tends to be lost following degradation. Polyphenols, which are naturally occurring molecules, can be employed as the fundamental units for the construction of metal-phenol networks[34,35]. It has been reported that phenols can chelate metals, resulting in LMCT, which in turn promotes antioxidant protection[34]. It is therefore postulated that the metal-ligand complex may act in a manner analogous to a natural enzyme following nanosheet degradation. Que, a molecule with a polyphenolic structure, is hypothesised to chelate with metal ions, thereby enhancing its antioxidant activity following degradation[36]. In order to verify that ions can be released after degradation of the nanosheets, an inductively coupled plasma (ICP) analysis was performed (Fig. 4a–d, Supplementary Figs. 8 and 9). The results demonstrated that the Cu^{2+} release of MON(Cu), MON(CuMn) and MON(CuMn)-Q persisted for up to 28 days without any abrupt release. It was noteworthy that the release amount of Cu^{2+} by MON(Cu) was greater than that of MON(CuMn) and MON(CuMn)-Q at the same time. MON(Cu), MON(CuMn) and MON(CuMn)-Q exhibited a rapid release of Cu^{2+} over a 24-hour period, with a subsequent gradual decline in the rate of release over time. The release pattern of Mn^{2+} was comparable to that of Cu^{2+}, although the quantity of Mn^{2+} released at 24 hours and 28 days was less than that of Cu^{2+} at the same time. To illustrate the chelating effect of que and metal ions, a fluorescence spectrophotometer was employed for further measurement. Que was uniformly dispersed in Phosphate Buffer Saline (PBS) and fluorescence was measured with excitation light at 425 nm and emission light between 450 and 800 nm. The results demonstrated the presence of a distinct peak when the emission light was ~628 nm (Supplementary Fig. 10). As the concentration of que increased, the fluorescence
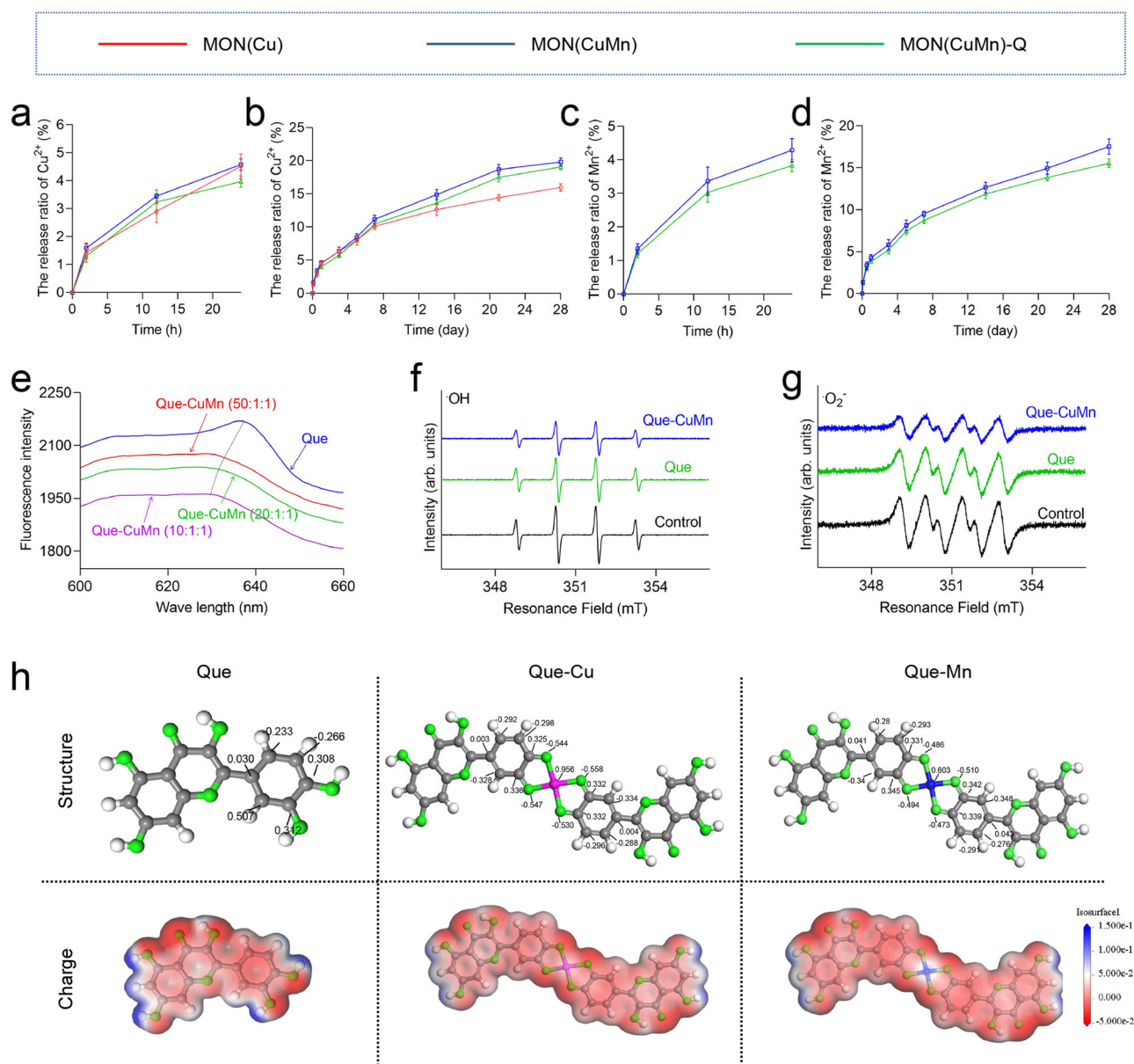
Fig. 4 | Antioxidation performance and mechanism of nanosheets after degradation. a, b The Cu^{2+} release ratio curves of MON(Cu), MON(CuMn), and MON(CuMn)-Q at 37 °C in PBS for short-term release (24 h) and long-term release (28 days), respectively, $n = 3$ independent experiments per group, data are expressed as mean ± SD. **c, d** The Mn^{2+} release ratio curves of MON(CuMn) and MON(CuMn)-Q at 37 °C in PBS for short-term release (24 h) and long-term release (28 days), respectively, $n = 3$ independent experiments per group, data are expressed as mean ± SD. **e** the curves of fluorescence spectrophotometer for que-metal chelates in different molar ratio. ESR spectra of (**f**) the Fenton reaction and (**g**) the XO + X reaction system for que-metal chelates. arb.units, arbitrary units. **h** The surface charge distribution and Mulliken charge transfer for que and que-metal chelates.

intensity increased, yet the position of the peak remained unchanged. Furthermore, the absorbance of solutions containing only Cu^{2+} or Mn^{2+} without que were measured and we found that there were no distinct peaks in the emission light region of 450-800 nm, suggesting that the peaks between 450-800 nm are specific to que. By measuring the peaks corresponding to different concentrations of que solutions and plotting the standard curves, it can be demonstrated that there is a proportional relationship between que concentration and fluorescence intensity within a certain concentration range (Supplementary Fig. 11a). Subsequently, the que content in MON(CuMn)-Q was quantified. Supplementary Fig. 11b demonstrated that the loading was 16.46 ± 0.72 μg/mL when que was fed at 25 μg/mL, 35.28 ± 1.06 μg/mL when que was fed at 50 μg/mL, and 68.41 ± 1.07 μg/mL when que was fed at 100 μg/mL. Furthermore, the release profile of que from

MON(CuMn)-Q was further measured (Supplementary Fig. 12). It was observed that the rate of que release was highest during the initial 24-hour period and subsequently declined. The release pattern of drugs exhibits some similarities to that of ions. This may be attributed to the fact that in the initial stages, drugs or ions that are not tightly bound are released rapidly, whereas in the later stages, due to the degradation of the material, a slow release of the drug or ion is achieved. To ascertain whether que can form complexes with metal ions, further measurements were conducted using a fluorescence spectrophotometer. Supplementary Fig. 13a illustrated that when the concentration of que remained constant, the addition of varying concentrations of copper ions resulted in a reduction in fluorescence intensity at the maximum peak. Furthermore, the addition of copper ions was observed to induce a blue shift in the fluorescence spectrum.

In contrast to copper ions, the addition of varying concentrations of manganese ions was observed to enhance the fluorescence intensity, resulting in a slight red shift of the peak value (Supplementary Fig. 13b). Finally, the result in Fig. 4e indicated that a gradual decrease in fluorescence intensity was accompanied by a blue shift of the peaks when que, copper and manganese ions were mixed in molar ratios of 50:1:1, 20:1:1 and 10:1:1. The absorption peaks of que in 628 nm are due to Π-Π* electron orbital transitions generated in the presence of enol structures, in accordance with literature reports[37–39]. After the chelation of copper ions with que, the fluorescence of que shows a decrease and a blue shift of the peak after chelation with copper ions, because copper ions reduce the degree of conjugation of the conjugated phenolic hydroxyl groups in the planar geometry of que molecules, which leads to a larger spatial site resistance[40]. As manganese ions contain more unpaired electrons, the system formed after chelation with que is more stable. Therefore, the energy required for the electron transition in the conjugated system is reduced after chelation, which is reflected in the increase of peaks and the red shift of the spectrum[41]. After the copper and manganese ions were both added to que solution at the same time, the degree of conjugation of phenolic hydroxyl group was reduced more obviously and the spatial site resistance increased because both copper and manganese ions could form chelates with que. In addition, the energy required for the Π-Π* electron orbital transition increases, thus showing a decrease in fluorescence and a blue shift of the peak value. In conclusion, the aforementioned results indicate that que is capable of forming chelates with metal ions, thereby altering the intrinsic properties of que. The antioxidant capacity of que and que-metal chelates were further examined using ESR spectroscopy. As illustrated in Fig. 4f, g, the characteristic signals of ·OH (1:2:2:1) and $\cdot O_2^-$ (2:2:1:2:1:2) were diminished, indicating that que-metal chelates had a greater ability to scavenge ROS compared to que. Furthermore, the SOD- and CAT-like activities of the que-metal chelates were evaluated at varying pH values, revealing that the chelates demonstrated antioxidant capacity across a range of pH conditions (Supplementary Fig. 14). However, no notable differences in the impact of pH on the SOD-like activity of the chelates were observed. Conversely, an excessively low or high pH could result in a reduction in CAT-like activity. The chelation of que with metals has the potential to enhance its antioxidant capacity, Fig. 4h illustrated the intrinsic mechanism. Theoretical calculations demonstrated that the 3',4'-o-hydroxyl group of que was capable of forming a chelate with metals. Following the calculation of the Mulliken charge (MC), it was determined that the redistribution of que surface charge could be facilitated by chelation with metals. Fig. 4h and Supplementary Fig. 15 also illustrated the electron static potential projection of que and que-metal chelate. The electrostatic potential charge (ESP) map demonstrated that the chelation of metals and que resulted in an uneven charge distribution, with a greater difference in electrostatic potential observed around copper ions in the que-copper chelate. Que can facilitate the transfer of protons through the phenolic hydroxyl group, thereby promoting the inactivation of free radicals. However, once the phenol is oxidised to benzoquinone, que is no longer capable of exerting its antioxidant effect[19,42]. In contrast, metal-chelated que can achieve a metal valence shift, thereby enabling a reaction similar to that of SOD and CAT, thus enhancing the antioxidant effect. Theoretical calculations of MC distribution indicated that the electron distribution of que chelated with copper and manganese ions was more heterogeneous than that of unchelated que. This suggested that que was more prone to undergo charge transfer by chelating copper and manganese ions, which in turn enhanced its antioxidant activity. As was illustrated in Supplementary Fig. 16, copper ions could facilitate the occurrence of CAT-like and SOD-like reactions through monovalent and divalent conversion while the chelation of copper could also regulate the electron distribution of que, favoring hydrogen donation to scavenge ·OH.

Antibacterial performance and mechanism

To investigate the ROS generation capacity of MON(CuMn) and MON(Cu) under US, ESR was used to detect ROS yield, where 2,2,6,6-tetramethylpiperidine (TEMP) was used as a single linear state oxygen probe. As shown in Fig. 5a, the $^1O_2$ characteristic signal (1:1:1) indicated that MON(CuMn) and MON(CuMn)-Q could generate more ROS compared to MON(Cu) under 1.5 W/cm² of US. Therefore, MON(CuMn) and MON(CuMn)-Q had a stronger SDT capacity than MON(Cu). This might be due to the fact that MnN₄ sites adsorbed O₂ and transferred electrons better than CuN₄. Notably, there was no significant difference in the ability of MON(CuMn)-Q to generate ROS under US compared to MON(CuMn), it was probably due to the reason that que loading would not change the ROS generation ability of MON(CuMn)-Q. In vitro antimicrobial experiments were used to further illustrate the differences in antimicrobial properties of different nanosheets. In order to ascertain the optimal concentration of nanosheets for antibacterial purposes, we initially conducted in vitro toxicity assessment experiments on nanosheets. The result of CCK8 demonstrated a progressive decline in cell survival as the concentration of nanosheets increased (Supplementary Fig. 17). While the tolerance of different cells to the nanosheets exhibited variability, it is notable that MON(Cu) at above 50 μg/mL, MON(CuMn) at above 100 μg/mL, and MON(CuMn)-Q at above 200 μg/mL demonstrated pronounced cytotoxicity. The IC50 results presented in Supplementary Fig. 18 demonstrated that MON(CuMn)-Q exhibited a lower degree of toxicity than MON(CuMn), whereas MON(Cu) was identified as the most toxic nanosheet. Furthermore, hemolysis experiment was conducted, which indicated that above 200 μg/mL of MON(CuMn)-Q may potentially cause the rupture of red blood cells (Supplementary Fig. 19). The impact of US on the cells was also evaluated independently. As illustrated in Supplementary Fig. 20, the addition of US (1.0 MHZ, 1.5 W/cm², 50% duty cycle, 15 min) could result in a reduction in the survival of hBMSCs while the cells were co-cultured with MON(CuMn)-Q. However, the functional state of the cells demonstrated a gradual recovery following US, with a survival rate comparable to that observed prior to US by day 14. This may be attributed to the nanosheets' ability to adsorb ROS and promote the recovery of cells. Subsequently, antimicrobial experiments were conducted on MON(CuMn)-Q with a concentration gradient, and the results demonstrated that the antimicrobial properties of the nanosheets were enhanced with increasing concentration (Supplementary Figs. 21 and 22). However, no significant difference was observed in the antimicrobial performance of MON(CuMn)-Q at 250 μg/mL and MON(CuMn)-Q at 200 μg/mL under US. This may be attributed to the fact that 200 μg/mL of MON(CuMn)-Q exhibits a high bactericidal rate under US, and the elevation of the concentration of the material does not significantly enhance the antibacterial performance. Subsequently, a comparison of the antimicrobial performance between different nanosheets was conducted. Given the aforementioned results, which indicated that above 200 μg/mL of MON(CuMn)-Q may damage cells and that below 200 μg/mL of MON(CuMn)-Q exhibited a suboptimal antimicrobial effect, a concentration of 200 μg/mL was selected as the antimicrobial concentration for subsequent materials. In addition, vancomycin was used to compare with nanosheets in terms of antimicrobial properties. The minimum inhibitory concentration (MIC) of vancomycin was 1 μg/mL[43,44]. To further compare the antimicrobial differences between vancomycin and different nanosheets, a uniform concentration of 200 μg/mL was employed. Fig. 5b illustrated the growth curves of bacteria in each group without US. As there was no US, the mechanism of the antibacterial effect of the nanosheets was mainly due to the release of ions or drugs. As both copper, manganese ions and que had an antibacterial effect, the bacteria in the material group showed growth inhibition compared to the control group. It is noteworthy that the antimicrobial properties of vancomycin at the same concentration were more pronounced than those of nanosheets. Moreover, it could be concluded that among nanosheets MON(Cu) had the highest
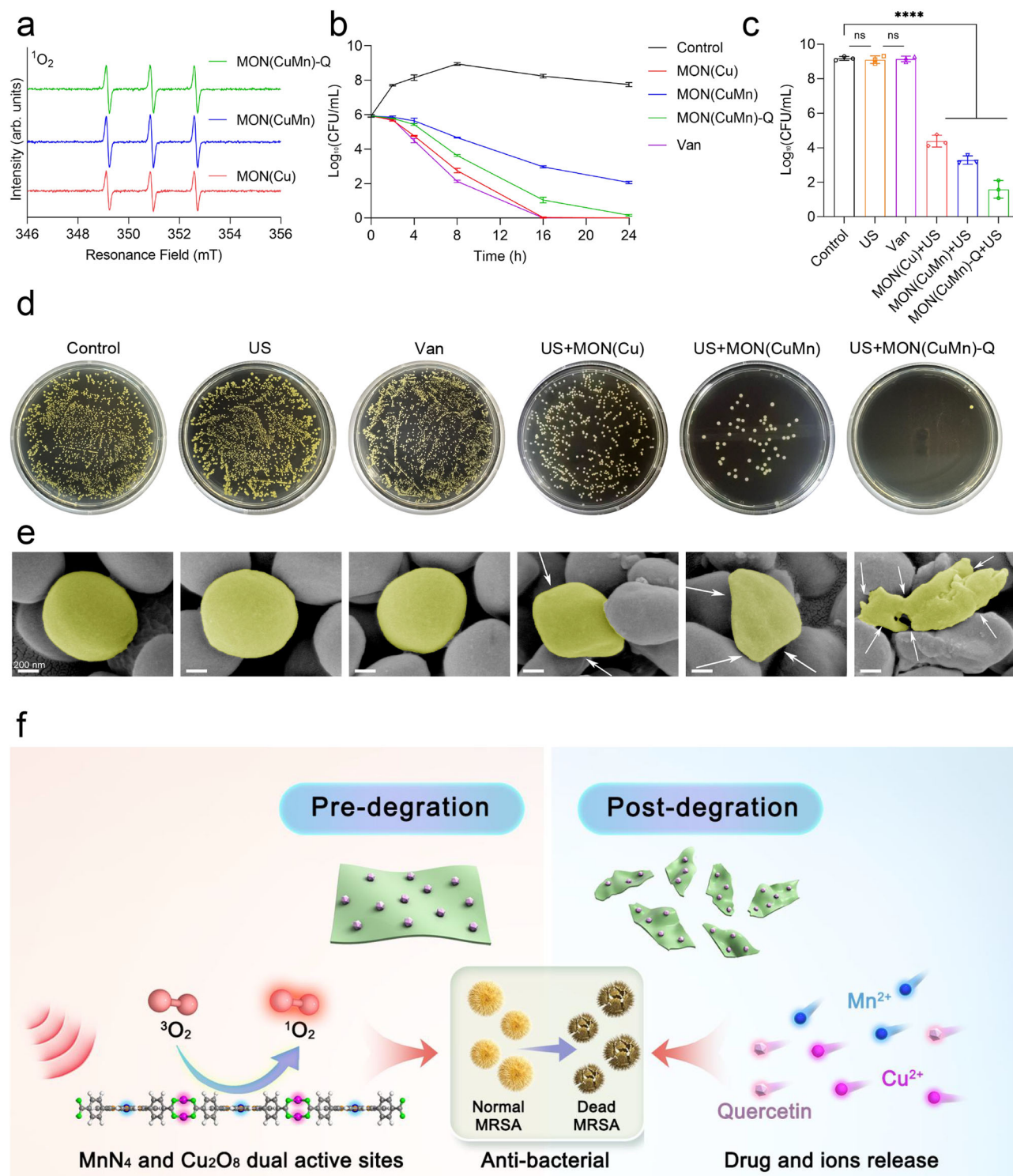
Fig. 5 | Antibacterial performance and mechanism of nanosheets before and after degradation. a ESR spectrum of $^1O_2$ under US. arb.units, arbitrary units. **b** Bacterial growth curve after different treatments, $n = 3$ independent experiments per group, data are expressed as mean ± SD. CFU, colony-forming units. **c** The number of MRSA colonies of the Control, US, Van, MON(Cu)+US, MON(CuMn)+US, MON(CuMn)-Q + US groups ($p = 0.6187$; $p = 0.8011$; $p < 0.0001$; $p < 0.0001$;

$p < 0.0001$), $n = 3$ independent experiments per group, data are expressed as mean ± SD, ****$p < 0.0001$, ns not significant, two-tailed ANOVA. CFU, colony-forming units. **d** Spread plate of MRSA colonies, three independent experiments were repeated. **e** SEM images of bacteria after different treatments. The morphology of bacteria is indicated by white arrows and marked in yellow colour, scale bar: 200 nm, three independent experiments were repeated. **f** Antibacterial mechanism.

antibacterial efficiency without US, while MON(CuMn) had the lowest antibacterial efficiency. We speculated that this was due to the fact that the number of copper ions released from MON(CuMn) and MON(C-uMn)-Q after degradation was lower than that of MON(Cu). There may be the following mechanisms for copper ions to exert an inhibitory

effect: 1) copper ions damage the bacterial cell membrane causing local oxidation which in turn promotes membrane rupture leading to bacterial death[2]; 2) copper ions may interact with components in the bacterial tricarboxylic acid cycle to promote death[23]. As another transition metal ion, Mn^{2+} has also been reported to have excellent antibacterial

properties[24]. However, our study found that Mn doped nanosheets would reduce the antibacterial efficiency in the absence of US. One reason might be that the antibacterial efficiency of Mn^{2+} was lower than that of Cu^{2+}. In addition, Mn^{4+} was reported to have almost no antimicrobial activity[45]. Another possible reason might be that the manganese-doped nanosheets in our study were found to enhance their antioxidant activity, which might have partially prevented oxidative damage to the bacteria. Since que also had certain antibacterial ability[22], the antibacterial activity of MON(CuMn) doped with que increased, but it was not stronger than MON (Cu). We speculated that on the one hand, the antibacterial ability was related to the amount of que loading, and on the other hand, the doping of que improved the antioxidant performance of the material to some degree. In conclusion, we showed that nanosheets could exert antimicrobial effects by releasing ions and drugs after degradation. Further investigation was conducted into the antibacterial properties of the nanosheets under US. Figs. 5c, d illustrated that MON(CuMn)-Q exhibited the strongest antibacterial activity, followed by MON(CuMn) and MON (Cu). In contrast, 200 μg/mL vancomycin does not exert a substantial antibacterial effect due to its limited action time. Despite both MON(CuMn)-Q and MON(CuMn) had almost the same ability to generate ROS under US from Fig. 5a, MON(CuMn)-Q demonstrated superior antibacterial activity. It was postulated that this might be due to the fact that US could simultaneously promote the release of que of MON(CuMn)-Q, and the release of the drug had a concomitant auxiliary bactericidal effect. To test this hypothesis, the quantity of Cu^{2+}, Mn^{2+} and que released from MON(CuMn)-Q following US was measured. The results demonstrated that US could indeed facilitate the release of ions or drugs (Supplementary Fig. 23), this may be due to the fact that US has a mechanical vibration effect that promotes the release of drugs or ions. As shown in Fig. 5e, the bacterial morphology after US treatment was further observed by SEM. The morphology of the bacteria in the control group was uniform in size, neatly arranged and smooth on the surface. US and vancomycin did not change the morphology of the bacteria, but the bacteria with the addition of nanosheets showed morphological changes, with the plasma membrane wrinkled, twisted and irregular (indicated by white arrows and yellow colour). The cell membrane damage was more severe in the MON(CuMn)-Q + US group compared to the MON(Cu)+US and MON(CuMn)+US groups. In conclusion, we have investigated the mechanism and effect of nanosheets in antibacterial performance (Fig. 5f). Before degradation, MON(CuMn)-Q can generate ROS through the dual active sites of MnN_4 and Cu_2O_8 under US, while after degradation, the released copper and manganese ions as well as que can exert antibacterial effects.

In vitro ROS scavenging and immunomodulatory ability

Oxidative stress represents a significant impediment to osteogenic repair[46]. ROS have been demonstrated to promote osteoclast senescence and death through the activation of osteoclast inflammatory signalling pathways[47]. Furthermore, they are shown to induce inflammatory polarisation of immune cells, which can in turn inhibit bone defect repair[48]. As illustrated in Supplementary Fig. 17 and Supplementary Fig. 18, an elevation in the concentration of the material could result in a reduction in cell viability. However, it is noteworthy that the nanosheets did not exhibit significant toxicity to the cells within a specific concentration range. Furthermore, it was observed that following the doping of manganese ion and que, the concentration of cell tolerance exhibited a gradual increase. This may be attributed to the observed improvement in the antioxidant properties of the materials. To ascertain whether the nanosheets could be effectively uptaken by cells, immunofluorescence (IF) was employed (Supplementary Fig. 24). By dye-labelling the nanosheets and co-culturing them with hBMSCs for three days, it was observed that the Cy5-labelled materials were distributed uniformly around the nuclei. Subsequently, the cells were stimulated with 100 μM H_2O_2 to induce oxidative stress and co-

cultured with nanosheets. DMTU, a clinically approved drug, has been demonstrated to be an effective scavenger of ROS[49]. Consequently, we employed DMTU and nanosheets for comparison. The ability of the nanosheets or DMTU to scavenge ROS within cells was further evaluated by staining the cells with 2,7-dichlorofluorescein diacetate (DCFH-DA). The result of the flow cytometry (FCM) demonstrated that the application of H_2O_2 resulted in an increase in the intracellular ROS content, whereas the nanosheets and DMTU exhibited a capacity to reduce the H_2O_2-induced ROS increase (Fig. 6a, Supplementary Figs. 25 and 26). Furthermore, the confocal results demonstrated that ROS could induce the crumpling and deformation of the cytoskeleton (Fig. 6b, c). However, MON(CuMn)-Q and DMTU could both effectively reduce the intracellular ROS content and restore the normal cytoskeletal arrangement. In comparison to other nanosheets, MON(CuMn)-Q exhibited a superior capacity to scavenge ROS. It is noteworthy that there was no significant difference in the ability of DMTU and MON(CuMn)-Q to scavenge ROS. Mitochondria represent a significant source of intracellular ROS, and the functional state of these organelles is indicative of the ROS levels within the cells[27]. To further investigate the functional state of cellular mitochondria, JC-1 was employed to label the cells, thereby reflecting the alterations in mitochondrial membrane potential. As illustrated in Fig. 6d and Supplementary Fig. 27, H_2O_2 stimulation resulted in the disruption of the cellular membrane potential, as evidenced by the accumulation of JC-1 monomers. In contrast, the use of nanosheets or DMTU improved the functional state of mitochondria and promoted the increase of JC-1 polymers. In conclusion, nanosheets could protect cells from oxidative stress. In comparison with other nanosheets, MON(CuMn)-Q has the strongest ability to remove ROS and is similar to DMTU.

The rate of wound healing in infected bone defects is closely correlated with the infiltration of inflammatory cells, particularly M1 macrophages[48]. The proliferation of M1 macrophages is induced by a variety of biological signals, including the presence of excess ROS. M1 macrophages secrete a range of inflammatory factors, including interleukin-6 (IL-6) and interleukin-1β (IL-1β), which damage cells at the wound site and impede the repair of bone defects[50]. It is therefore hoped that the ROS level in M1 macrophages can be reduced by nanosheet uptake, thus changing the pro-inflammatory M1 phenotype of macrophages to the anti-inflammatory M2 phenotype, and promoting the treatment of bone defects. Following the differentiation of the cell line human acute monocytic leukemia cells (THP1) into macrophages using phorbol 12-myristate 13-acetate (PMA), the anti-inflammatory effect of the nanosheets was further observed. The cells were initially incubated with LPS for a period of two days in order to induce the M1 phenotype. Subsequently, the cells were co-cultured with PBS or nanosheets or DMTU for a further two days. Supplementary Figs. 28 and 29 illustrated that the nanosheets and DMTU were capable of reducing the level of ROS in THP1 following stimulation with LPS. Furthermore, nanosheets and DMTU were demonstrated to stabilize mitochondrial membrane potential and protect THP1 from oxidative stress (Supplementary Fig. 30). The confocal results showed that both nanosheets and DMTU could promote the decrease of JC-1 monomers and the increase of polymers (Supplementary Fig. 31). These findings suggested that nanosheets could mitigate the rise in endogenous ROS triggered by LPS and maintain mitochondrial membrane potential. Among the nanosheets, MON(CuMn)-Q displayed the most pronounced effect and exhibited a profile comparable to that of DMTU. CD86 and CD206 are markers of macrophage M1 and M2 polarization, respectively[48]. As illustrated in Fig. 6e–g, Supplementary Figs. 32 and 33, LPS treatment could induce the polarization of THP1 to the M1 phenotype. Conversely, scavenging ROS could facilitate the reprogramming of M1 THP1 to M2. The results demonstrated that MON(CuMn)-Q exhibited excellent antioxidant properties and a pro-macrophage M2 programming effect similar to DMTU (Fig. 6h).
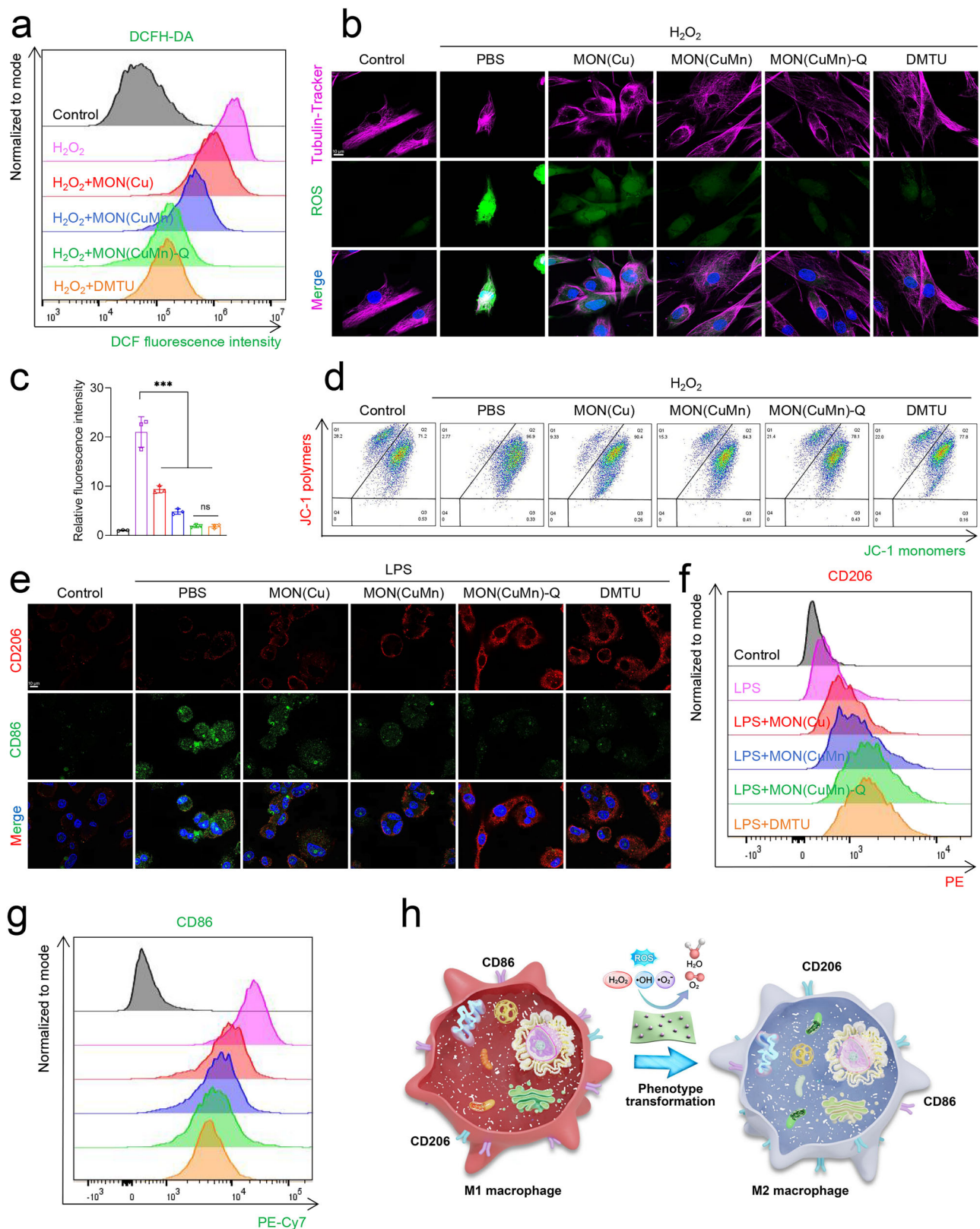
Fig. 6 | In vitro ROS scavenging and immunomodulatory ability. a FCM analysis of DCFH-DA. **b** Representative images of DCFH-DA staining in hBMSCs after different treatment, scale bar: 10 μm, three independent experiments were repeated. **c** Statistical result of DCFH-DA staining ($p = 0.0009$; $p = 0.0009$; $p = 0.0004$; $p = 0.0004$; $p = 0.9208$), $n = 3$ independent experiments per group, data are expressed as mean ± SD. ***$p < 0.001$, two-tailed ANOVA. **d** FCM result of JC-1. **e** IF result of polarization in THP1, scale bar: 10 μm, three independent experiments were repeated. **f**, **g** FCM analysis for polarization condition of THP1. **h** Graphic illustration of MON(CuMn)-Q in immunomodulatory ability.

In vitro osteogenesis and angiogenesis ability

In order to explore the potential of nanosheets in repairing wound and bone tissue, the angiogenesis and osteogenesis abilities of nanosheets were measured in vitro. Human bone marrow mesenchymal stem cells (hBMSCs) were co-cultured with nanosheets, after which alkaline phosphatase (ALP) and Alizarin Red S (ARS) staining was performed on day 14 and day 21, respectively (Fig. 7a). The ALP staining was found to

be significantly more pronounced in the MON(CuMn)-Q group compared to that of the control, MON(Cu) and MON(CuMn) groups. The results of ARS staining were also consistent with those observed in ALP staining. The mineral nodules in the nanosheet groups were found to be significantly higher than in the control group, with the highest levels observed in the MON(CuMn)-Q group. These findings indicated that nanosheets may enhance the osteogenic potential of hBMSCs. This

Fig. 7 | In vitro osteogenesis and angiogenesis ability. a ARS and ALP staining images of hBMSCs under different culture conditions: culture medium (denoted as Control), MON(Cu) containing medium (denoted as MON(Cu)), MON(CuMn) containing medium (denoted as MON(CuMn)) and MON(CuMn)-Q containing medium (denoted as MON(CuMn)-Q), scale bar: 200 μm, three independent experiments were repeated. **b** Volcano map of RNA-seq result (MON(CuMn)-Q vs Control). **c** GO analysis of up-regulated genes in MON(CuMn)-Q. **d** IF result of hBMSCs after 28 days of culture under different conditions, scale bar: 200 μm, three independent experiments were repeated. **e, f** Scratch test and statistic analysis of HUVECs ($p < 0.0001$; $p = 0.0001$; $p = 0.0003$), scale bar: 200 μm, $n = 3$ independent experiments per group, data are expressed as mean ± SD. ***$p < 0.001$, ****$p < 0.0001$, two-tailed ANOVA. **g–i** WB and corresponding statistic analysis of HIF-1a ($p < 0.0001$; $p < 0.0001$; $p < 0.0001$) and VEGFA ($p = 0.0002$; $p = 0.0001$; $p = 0.0006$), $n = 3$ independent experiments per group, data are expressed as mean ± SD. ***$p < 0.001$, ****$p < 0.0001$, two-tailed ANOVA. **j–l** Tube formation and statistic analysis of relative tube length ($p = 0.0037$; $p = 0.0033$; $p = 0.0039$) and relative junction number ($p = 0.0009$; $p = 0.0042$; $p = 0.0042$), scale bar: 200 μm, $n = 3$ independent experiments per group, data are expressed as mean ± SD. **$p < 0.01$, ***$p < 0.001$, two-tailed ANOVA. **m** qRT-PCR results of HIF-1a and VEGFA in HUVECs after different treatments, $n = 3$ independent experiments per group.

effect may be attributed to the osteogenic properties of copper ions, manganese ions and que[36,51,52]. In order to elucidate the mechanism by which MON(CuMn)-Q promotes osteogenesis, RNA sequencing was employed on hBMSCs. Two groups were established, comprising the control and MON(CuMn)-Q groups. The control group was maintained in a continuous culture of medium lacking any material for a period of 21 days, while the MON(CuMn)-Q group was subjected to a 21-day culture in a medium containing 150 μg/mL MON(CuMn)-Q. Following this, both groups underwent RNA sequencing. The volcano map was employed to analyze the differential genes of the control and MON(CuMn)-Q groups, and the results demonstrated that a total of 2616 genes were significantly down-regulated and 1975 genes up-regulated in the MON(CuMn)-Q group in comparison to the control group (Fig. 7b). A search was conducted for genes related to osteogenic differentiation, and it was found that the SPP1, RUNX2, SP7, BMP2 and ALPL genes were significantly increased in the MON(CuMn)-Q group (Supplementary Fig. 34). Subsequently, the Gene Ontology (GO) terms were analyzed, and several GO terms associated with cell differentiation under MON(CuMn)-Q co-culture were identified (Fig. 7c). To further elucidate the pathway involved in bone differentiation, Kyoto Encyclopedia of Genes and Genomes (KEGG) enrichment analysis was conducted. As illustrated in Supplementary Fig. 34, MON(CuMn)-Q was found to activate JAK-STAT, PI3K-AKT, Wnt, MAPK and TGF-β pathways, which play a significant role in osteogenesis. Western blot (WB) and IF were employed to corroborate the findings of RNA sequencing. The results demonstrated that nanosheets facilitated osteogenic differentiation of hBMSCs, with MON(CuMn)-Q exhibiting the most pronounced effect (Fig. 7d, Supplementary Figs. 35 and 36).

It has been reported that copper ions can promote angiogenesis, and thus we hypothesize that nanosheets have a significant angiogenic potential[53]. To test this hypothesis, a scratch assay was conducted. After 6 hours of co-culture, the nanosheets were observed to significantly enhance the migration of umbilical vein endothelial cells (HUVECs) (Fig. 7e, f). Furthermore, the tube formation experiment demonstrated that the capacity of HUVECs to form tubes could be markedly augmented by culturing them for three days in a medium containing nanosheet (Fig. 7j–l). The HIF-1a/VEGFA pathway is a significant mediator of angiogenesis[54]. However, the role of this pathway in nanosheet-mediated treatment remains unclear. To ascertain whether this pathway is activated, WB, IF and quantitative Real-Time fluorescence Polymerase Chain Reaction (qRT-PCR) were employed, and it was found that HIF-1a/VEGFA could be upregulated in HUVECs by nanosheet treatment, which reflected the angiogenesis of the materials (Fig. 7g–i, m and Supplementary Fig. 37).

In conclusion, the experimental results described above indicated that the nanosheets had favourable angiogenic and osteogenic effects. These effects might be attributed to the release of copper-manganese ions and que.

In vivo treatment of infected cranial defects

Further investigation was conducted to examine the SDT effect of MON(CuMn)-Q on infected critical-sized defects using a rat model of cranial defects infected by MRSA. In order to prolong the time that the material remains in the defect, gels were used in our experiment.

Jelleine-1 (Je-1) is a typical amphiphilic antimicrobial peptide, first isolated from royal jelly with the sequence Pro-Phe-Lys-Ser-Leu-His-Leu-NH2 (952.59 Da)[55]. It has temperature-sensitive gel-forming properties and can self-assemble to form gels at suitable concentrations[56]. MON(CuMn)-Q was encapsulated into Je-1 (MON(CuMn)-Q-J) for further treatment. As illustrated in Supplementary Fig. 38, the gel structures could be efficiently formed using 4 mg/L Je-1 incubated at 37°C for 15 minutes. The surface morphologies of Je-1 and MON(CuMn)-Q-J were further observed by SEM, and the results demonstrated the presence of uniform nanoribbons or nanobundles, which indicated that the nanofibers could aggregate and cross-link (Supplementary Fig. 39). The above results demonstrated the successful preparation of the antibacterial gel containing MON(CuMn)-Q. A 6-mm hole was created in the rat's skull using a trephine, after which either PBS (the Control group) or MRSA bacterial solution was injected into the defect site. Following a three-day interval, the MRSA-infected rat wounds were reopened and PBS (the MRSA group) or MON(CuMn)-Q-J (the MON(CuMn)-Q-J + US group) was injected into the skull defects. The MON(CuMn)-Q-J + US group underwent US irradiation (1.5 W/cm², 50% duty cycle, 1 MHz) for 15 minutes. Intravenous vancomycin represents the gold standard for the clinical treatment of MRSA infection[43,57]. Additionally, 40 mg/kg has been reported to be the most commonly used dosage for the treatment of infected bone defects in rats[8,10]. Consequently, we administered 40 mg/kg of vancomycin intravenously into rats after three days of infection (the Van group), with the aim of comparing the results with those of the MON(CuMn)-Q-J + US group. Acute toxicity experiments were used to determine the concentration of material used before formal experiments began. We used different concentrations of MON(CuMn)-Q encapsulated in Je-1 gel and collected serum from rats 7 days after treatment to examine liver and kidney functions. The results showed that MON(CuMn)-Q above 200 μg/mL may have some hepatorenal toxicity (Supplementary Fig. 40). In addition, the sonozyme may come into direct contact with the skin due to the large skin opening of the rats in the cranial infection defect model. To investigate the dermal irritation of the material, we performed intradermal irritation tests in rabbits. As shown in Supplementary Fig. 41, above 200 μg/mL of MON(CuMn)-Q injected intradermally caused some skin irritation in rabbits, and erythema and oedema were visible on the skin. In light of the limited antimicrobial efficacy of below 200 μg/mL of MON(CuMn)-Q and the associated toxicity above 200 μg/mL, the final decision was taken to utilise 200 μg/mL of MON(CuMn)-Q in the animal experiment. The experimental flow chart is shown in Fig. 8a. As illustrated in Fig. 8b, images of the muscles surrounding the wound were obtained after 14 days of treatment. It was observed that significant abscesses were present in the MRSA group, whereas no such abscesses were observed in the other groups. Gram-stained images of muscle tissue near the infection demonstrated the absence of significant dark blue Gram-positive bacteria in the MON(CuMn)-Q-J group on day 7 post-treatment (indicated by yellow arrows). Notably, no dark blue bacteria were observed in the Van group until day 14, suggesting that the antimicrobial capacity of MON(CuMn)-Q-J was superior to that of vancomycin (Fig. 8c and Supplementary Fig. 42). To investigate the level of inflammatory infiltration at the wound site, haematoxylin and eosin (H&E) staining was
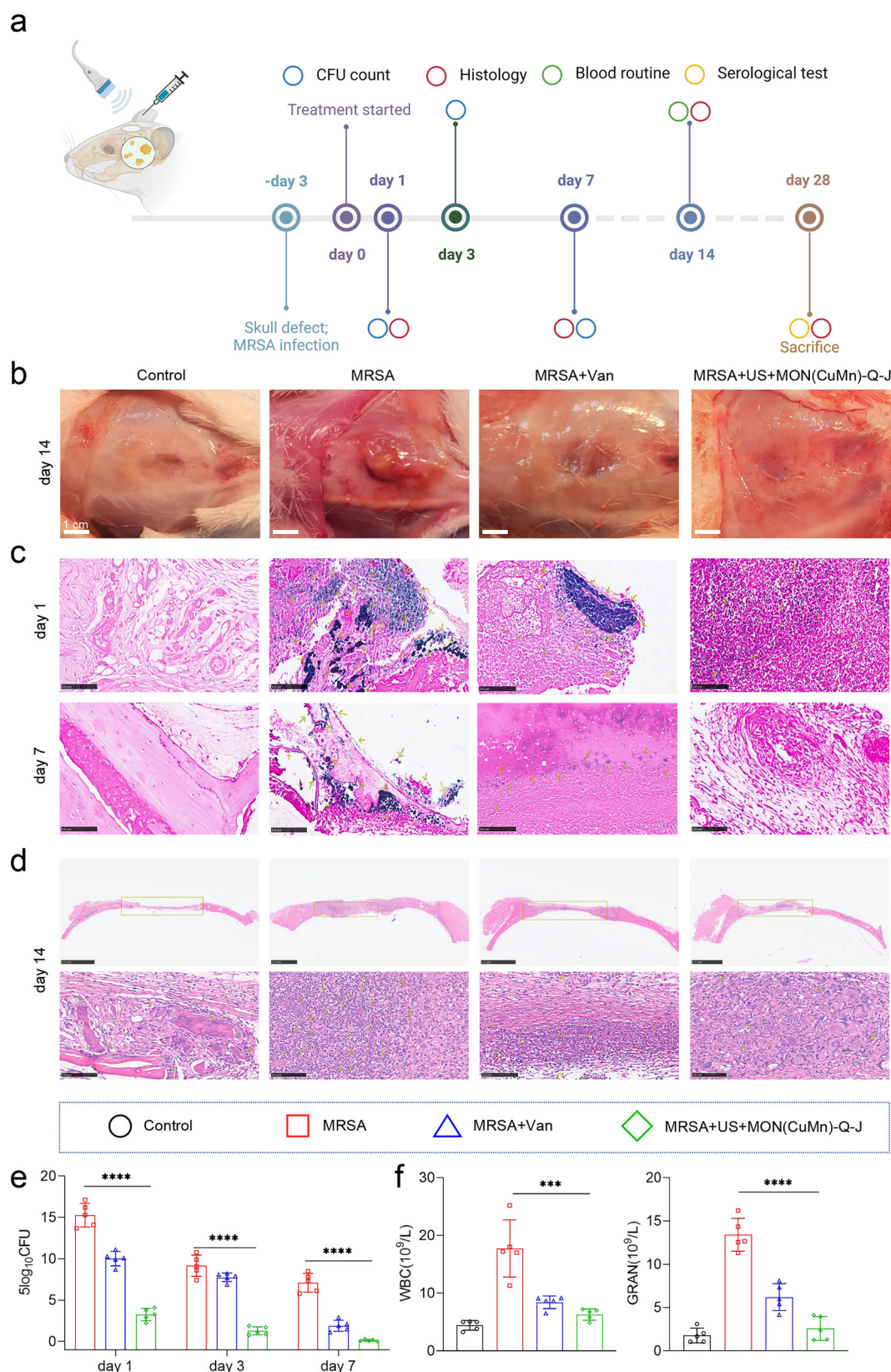
performed on infected bone tissue. As illustrated in Fig. 8d, there was a considerable number of inflammatory cells in the MRSA group, whereas the inflammatory infiltration was significantly reduced in the MON(CuMn)-Q-J + US group (indicated by yellow arrows). Further evaluation of the surgical site was conducted by collecting granulation tissues to assess for the presence of bacterial infection. Fig. 8e and

Supplementary Fig. 43 illustrated that, in comparison to the MRSA group, MON(CuMn)-Q-J significantly reduced the number of colonies. Furthermore, a white blood cell (WBC) test was conducted on day 14 post-treatment, which revealed that the WBC and granulocyte (GRAN) numbers were lower in the Control, VAN, and MON(CuMn)-Q-J + US groups compared to the MRSA group (Fig. 8f). However, no significant

Fig. 8 | In vivo antibacterial performance in infectious cranial defects. a The flow chart of animal experiment (Created in BioRender. Zixuan, O. (2024) https://BioRender.com/z84t695). **b** Photographs of wound appearance in rats on day 14 after treatment, scale bar: 1 cm, five independent experiments were repeated. **c** Gram staining of tissue slices on day 1 and day 7 after treatment. MRSA is indicated by yellow arrows, scale bar: 100 μm, five independent experiments were repeated. **d** H&E result of tissue slices on 14 day after treatment. Inflammatory cells are indicated by yellow arrows, scale bar: 2.5 mm, five independent experiments

were repeated. **e** CFU counts of MRSA in infected tissue homogenate ($p < 0.0001$; $p < 0.0001$; $p < 0.0001$), $n = 5$ independent experiments per group, data are expressed as mean ± SD. ****$p < 0.0001$, two-tailed ANOVA. CFU, colony-forming units. **f** Blood routine examination of rats after 14 days ($p = 0.0009$; $p < 0.0001$), $n = 5$ independent experiments per group, data are expressed as mean ± SD. ***$p < 0.001$, ****$p < 0.0001$, two-tailed ANOVA. WBC, white blood cell count. GRAN, granulocyte count.

difference was observed between the Control and the MON(CuMn)-Q-J + US groups. To exclude that the antimicrobial results were due to Je-1, we also evaluated the antimicrobial effect of Je-1. Je-1 and MON(CuMn)-Q-J were injected into the defects and the surrounding tissues were collected for spread plates on the first, third and seventh days after treatment. The results showed that Je-1 had some antimicrobial effect compared to the MRSA and the US groups, but the effect was not strong and much smaller than that of the MON(CuMn)-Q-J group (Supplementary Fig. 44). In addition, Gram staining suggested that the antibacterial ability of Je-1 was much weaker than that of MON(CuMn)-Q-J (Supplementary Fig. 45). In conclusion, the results demonstrated that MON(CuMn)-Q-J had excellent antibacterial and anti-inflammatory effects.

To investigate the osteogenic effect of MON(CuMn)-Q-J, a micro-CT analysis of the skull was performed on day 28 post-treatment. As illustrated in Fig. 9a, MRSA infection resulted in bone destruction around the site of the bone defect. However, the bone was restored with vancomycin and MON(CuMn)-Q-J + US treatment, with the size of the cranial defect being smaller in the MON(CuMn)-Q-J + US treatment than in the vancomycin group or even in the control group. In order to further elucidate the impact of MON(CuMn)-Q-J on bone repair of infected skull defects, the bone volume/total volume (BV/TV) was calculated on the 28th day following treatment. The results demonstrated that MON(CuMn)-Q-J exhibited the most efficacious bone repair effect, even surpassing that of the control and Van groups (Fig. 9b). Infected skull defects treated with MON(CuMn)-Q-J exhibited greater new bone formation than the other three groups, as evidenced by Masson staining (Fig. 9c). The majority of the new bone formed after MON(CuMn)-Q-J treatment was mature and fully mineralized cancellous bone (blue staining), whereas no significant new bone formation was observed in the infected group. OPN expression was observed by immunohistochemistry (IHC), and it was found that the MON(CuMn)-Q-J + US group exhibited the deepest colouration, while the infected group exhibited the least OPN expression (Fig. 9d). Further investigation by IF of osteogenic proteins (OPN and RUNX2) around the surgical site revealed that these proteins were more likely to be expressed at cranial defects after treatment with MON(CuMn)-Q-J. This suggested that MON(CuMn)-Q-J had superior osteogenic capacity (Fig. 9e and Supplementary Fig. 46). Furthermore, the osteogenic capacity of Je-1 was also assessed. CT revealed that Je-1 exhibited some osteogenic potential, albeit to a lesser extent than MON(CuMn)-Q-J (Supplementary Fig. 47). Additionally, BV/TV yielded comparable outcomes (Supplementary Fig. 47). It is postulated that the osteogenic impact of Je-1 may be attributed to its antimicrobial activity. To further observe the angiogenesis ability of the material, bone tissue was collected, and IF was performed. The results demonstrated that the skull treated with MON(CuMn)-Q-J exhibited high expression of vascular proteins, including CD31 and VEGFA, which were significantly higher than those observed in the other three groups (Fig. 9f and Supplementary Fig. 48). It has been reported that iNOS and CD206 are the M1 and M2 polarization markers of macrophages, respectively[48]. In Fig. 9g and Supplementary Fig. 49, IF was performed to observe the immunomodulatory capacity of MON(CuMn)-Q-J, and the results indicated that MON(CuMn)-Q-J could effectively promote the M2 polarization of macrophages, while M1 polarization was more easily promoted after MRSA infection. In conclusion, MON(CuMn)-Q-J exhibits remarkable

osteogenic, angiogenic, and immunoregulatory properties. Furthermore, histological examination of the heart, liver, spleen, and kidney revealed no discernible lesions, indicating that MON(CuMn)-Q-J exhibited minimal toxicity to major organs (Supplementary Fig. 50). In order to assess the renal function of rats, blood samples were collected on day 28 following the treatment. The measurement of creatinine, uric acid, and urea indicated that MON(CuMn)-Q-J did not induce nephrotoxicity in rats (Supplementary Fig. 51).

Discussion

The treatment of critical-sized bone defects is challenging due to the extensive range of the defect and the often associated drug-resistant bacterial infections. The utilisation of degradable materials with SDT ability has the potential to enhance bactericidal activity through the elevation of ROS levels. However, excess ROS levels may also aggravate inflammation and impede osteogenic healing. Moreover, a significant proportion of degradable materials are reliant on active sites for their functionality. Consequently, their efficacy is diminished over time as they degrade. In order to address the aforementioned issues, we have developed a Janus sonozyme to eliminate bacteria and promote bone regeneration. In contrast to traditional degradable materials, the sonozyme demonstrates the capacity to regulate ROS levels and to exert a prolonged antibacterial and anti-inflammatory effect within the defects. Prior to degradation, the material can adsorb ROS through dual active sites and simultaneously generate ROS under US, exerting antibacterial effects. Following degradation, the material can exert antimicrobial capacity through ion and drug release, and also strengthen the antioxidant effect of que through metal-phenol chelation. Finally, the potent antioxidant and antimicrobial capacity of the material was confirmed in a model of infective skull defects in rats. Although surgical debridement and antibiotic flushing are the standard treatments for infected bone defects, surgical debridement can exacerbate bone defects, and antibiotic treatment is prone to the risk of drug resistance. In contrast, this Janus sonozyme was developed with the objective of rapidly combating infection and inflammation, thereby facilitating the rapid repair of bone tissue. Nevertheless, further testing in large animals is required to assess the therapeutic efficacy and toxicity of the sonozyme. In conclusion, we have developed a continuous antibacterial and anti-inflammatory biodegradable material with the objective of achieving efficient treatment of infected critical-sized bone defects.

Methods
Chemicals
N, N-dimethylformamide (DMF), ethanol, tetrakis (4-carboxyphenyl) porphyrin (TCPP), Manganese tetrakis (4-carboxyphenyl) porphyrin (TCPP(Mn)), Manganese chloride tetrahydrate ($MnCl_2 \cdot 4H_2O$), Copper nitrate trihydrate ($Cu(NO_3)_2 \cdot 3H_2O$), and trifluoroacetic acid (TFA) were purchased from Aladdin. Polyvinylpyrrolidone (PVP) and que were purchased from Sigma-Aldrich.

Preparation of MON(Cu), MON(CuMn) and MON(CuMn)-Q
TCPP (16 mg, 0.02 mmol) was added to 48 ml DMF solution and heated with stirring until the solution was free of particles. $Cu(NO_3)_2 \cdot 3H_2O$ (14.4 mg, 0.06 mmol) and TFA (0.16 mmol) were then added to 16 ml of ethanol and stirred well. Finally, the mixture of DMF and ethanol solution was placed in a muffle furnace, heated to 80 °C at 2 °C/min
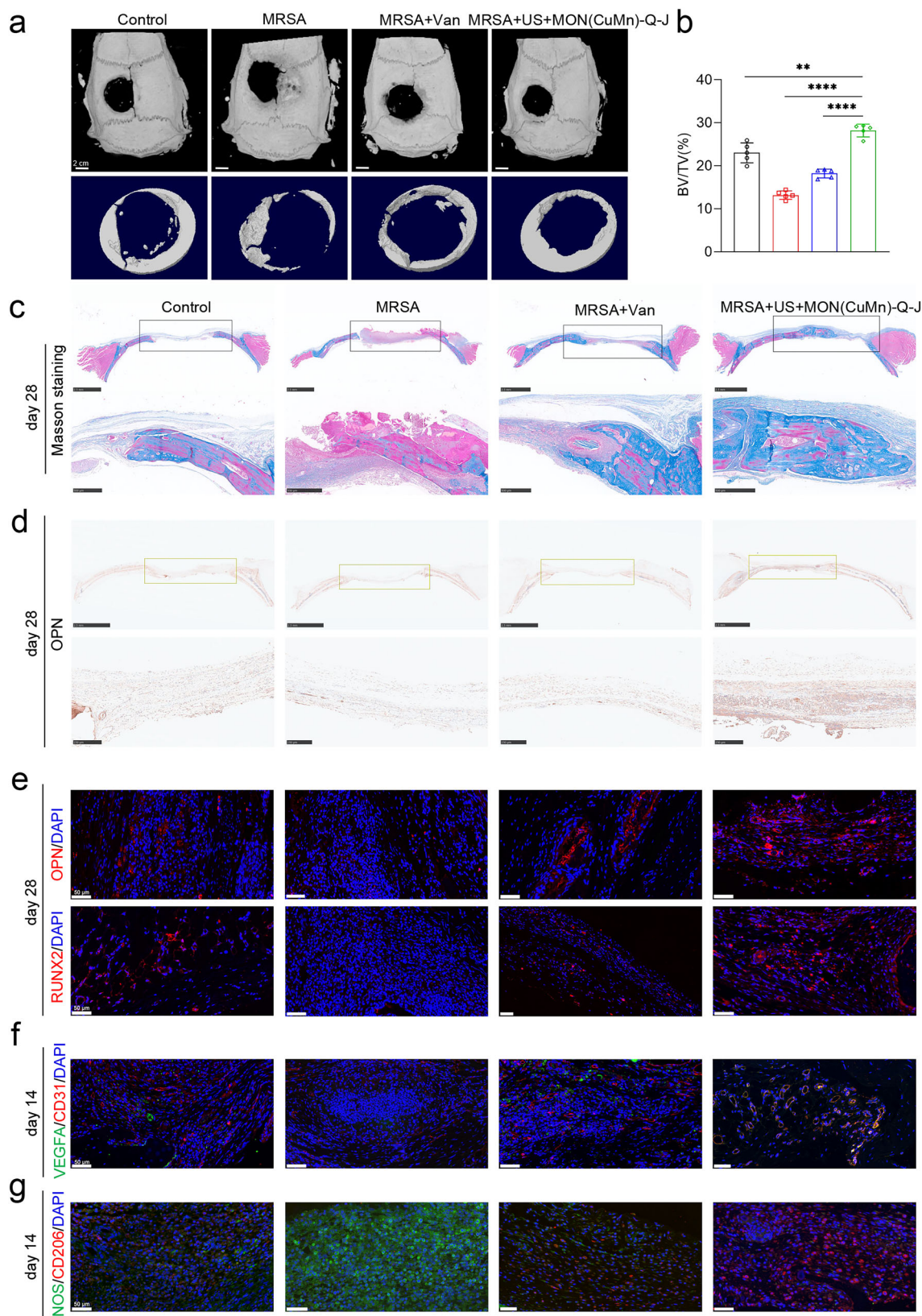
and held for 4 h. The products were washed with ethanol, centrifuged three times (7500 × g for 10 min each time) and finally dried. In order to obtain MON(CuMn), the TCPP in the above step could be replaced with TCPP(Mn) (17 mg, 0.02 mmol). To prepare MON(CuMn)-Q loaded with different concentrations of que, 25 μg/mL, 50 μg/mL, and 100 μg/mL of que were mixed with 200 μg/mL of MON(CuMn), respectively, and stirred for a period exceeding 12 hours at room temperature. Finally, the probe sonication (JY92-IIN, Ningbo Scientz Biotechnology Co. LTD) was employed for 30 min at power density of 130 W to generate the smaller nanosheets.

Characterization

A filed-emission scanning electron microscope (FE-SEM, S-4800, Hitachi) and TEM (JEOL-2100F, Japan Electronics Co., Ltd) were used to obtain morphology characterization. To measure the thickness of each nanosheet, the AFM (Agilent 5500, Bruker Dimension Icon) was applied. The elemental composition and chemical state of the nanosheets were determined by XPS (Escalab 250Xi, Thermo Fisher Scientific).

Que-metal chelate measurement

Firstly, que solutions of 20, 50, 100, 200 and 500 µg/mL were prepared by uniformly dispersing que in PBS. Subsequently, the preparation of que and Cu^{2+} chelates was conducted by the addition of $Cu(NO_3)_2 \cdot 3H_2O$ to a solution of que at a concentration of 100 µg/mL. The molar ratios of que to Cu^{2+} were varied, with the ratios set at 2:1, 5:1, 10:1, 20:1, 50:1, and 100:1. The que and Mn^{2+} chelates were prepared in a manner analogous to that described above, with $MnCl_2 \cdot 4H_2O$ added to a solution of que at a concentration of 100 µg/mL. The molar ratios of que and Mn^{2+} were varied, with the aim of investigating the effects of these ratios on the properties of the chelates. Molar ratios of 2:1, 5:1, 10:1, 20:1, 50:1, and 100:1 were employed. Finally, to prepare the chelates of que, Cu^{2+} and Mn^{2+}, a solution of 100 µg/mL que was used and $MnCl_2 \cdot 4H_2O$ and $Cu(NO_3)_2 \cdot 3H_2O$ were added to achieve molar ratios of 10:1:1, 20:1:1, and 50:1:1 for que, Cu^{2+}, and Mn^{2+}, respectively. The absorbance of the solutions was quantified using a fluorescence spectrophotometer (Shanghai Mepda Instrument Co., Ltd.). The instrument was operated with a PMT voltage of 700 V, a scanning speed of 1,500 nm/min, and a response time of 0.4 s. Excitation light at 425 nm and emission light between 450 nm and 800 nm were employed.

Antioxidant performance

The nanosheets were homogeneously dispersed into PBS at a concentration of 200 µg/ ml. Subsequently, the $\cdot O_2^-$ scavenging ratio and CAT-like activity were measured according to the manufacturer's protocols (BC0205, Solarbio; S0109, Beyotime). In addition, to further investigate the $\cdot O_2^-$ and $\cdot OH$ scavenging abilities of nanosheet and que-metal chelates, XPS was performed using DMPO as the spin trapping reagent. Briefly, 10 mM xanthine, 0.5 U XO, 10 mM DMPO and each nanosheet were added into the methyl alcohol solutions for $\cdot O_2^-$ detection. Then an aliquot of the solution (100 µL) was transferred into the quartz tube for ESR (JES-FA200, Japan Electronics Co., Ltd) measurements. To detect $\cdot OH$, 5 mM H_2O_2, 2 mM $FeSO_4$, 50 mM DMPO, and each nanosheet were added into the PBS solutions and 100 µL of the solution was used for ESR measurement. For que-metal chelates, a 2 mg/mL solution of que was first prepared with water or methanol. After that, 1 mL of que solution was taken and 0.13 ml of 0.2 mg/mL $MnCl_2 \cdot 4H_2O$ solution and 0.16 ml of 0.2 mg/mL $Cu(NO_3)_2 \cdot 3H_2O$ solution were added. After mixing, 10 µL was taken for ESR determination. To further investigate the ability of nanosheets or chelates to scavenge ROS at different PH values, we added 1 M HCl or NaOH and used a pH meter to adjust the final solution pH to 5.8, 7.8, and 9.8 before measuring with the kits or ESR.

Ion release measurement

The MON(Cu), MON(CuMn) and MON(CuMn)-Q solutions (200 µg/mL) were incubated at 37 °C for short (0, 2, 12 and 24 h) and long (3, 5, 7, 14, 21 and 28 d) periods. Afterwards, the supernatants were collected and the release of ions was measured using inductively-coupled plasma atomic emission spectrometry (ICP-AES, Optimal 8000, Perkin-Elmer), inductively coupled plasma optical emission spectrometry (ICP-OES, Vista-MPX, Varian) and inductively coupled plasma mass spectrometry (ICP-MS, Agilent 7800 Series). In order to detect the content of Cu^{2+} and Mn^{2+} in MON(Cu), MON(CuMn) and MON(CuMn)-Q, concentrated nitric acid was added to a solution of nanosheets at a concentration of 200 µg/mL and finally stored at 60 °C for 12 hours. Following this, the solution was measured using the instrument.

In order to ascertain whether US has an impact on ion release, we proceeded to take the nanosheet solutions both before and after US, and subsequently incubate them at 37 °C for a period of 2, 12 and 24 hours. The US parameter was: 1.5 W/cm², 50% duty cycle, 15 min. After centrifugating at 25,000 × g for 15 min, the resulting supernatants were then employed for ICP measurements.

Quercetin release measurement

Firstly, the spectra of standard que solutions were measured using a fluorescence spectrophotometer (Shanghai Mepda Instrument Co., Ltd.). Fluorescence intensity was recorded at an excitation light of 425 nm and an emission light of 450 nm to 800 nm. The MON(Cu), MON(CuMn) and MON(CuMn)-Q solutions (200 µg/mL) were incubated at 37 °C for varying periods of time, namely 0, 2, 12 and 24 hours for the short incubation period, and 3, 5, 7, 14, 21 and 24 hours for the long incubation period. The precipitate was removed by centrifugation at 25,000 × g for 15 minutes, after which the supernatant was taken for spectroscopic determination. The que content was calculated by measuring the maximum fluorescence intensity of the supernatant.

To ascertain the quantity of que loaded on the MON(CuMn)-Q, MON(CuMn)-Q solution was incubated for a period of 6 hours and subsequently subjected to centrifugation at 25,000 × g for 15 minutes. The supernatant was then taken for spectroscopic determination. The que loaded on the MON(CuMn)-Q was estimated by subtracting the amount of que present in the supernatant from the total amount of feed.

In order to ascertain the impact of US on the release of que from the nanosheets, 200 µg/mL of nanosheets were employed in the experiments. The US parameters employed were as follows: 1.0 MHZ, 1.5 W/cm², 50% duty cycle, 15 min. The MON(CuMn)-Q solution were then incubated at 37 °C for a period of 2, 12 and 24 hours. Following this, the supernatants were collected for fluorescence intensity measurement.

Theoretical calculations

Spin-polarised first-principle calculations were performed using the density functional theory (DFT) with the Vienna Ab-initio Simulation Package (VASP)[58]. The electronic exchange and correlation effects were described using the generalized gradient approximation (GGA) with the Perdew-Burke-Ernzerhof (PBE) functional[59–61]. A uniform G-centered k-points mesh with a resolution of $2\pi \times 0.05$ Å^{-1} and Methfessel-Paxton electronic smearing were employed for the integration in the Brillouin zone during the geometric optimisation process. throughout the computations, a cutoff energy of 500 eV was utilised. These settings ensure convergence of the total energies to within 1 meV per atom. The structure was relaxed until all forces on the atoms were less than 10 meV Å^{-1}, and the total stress tensor was within 0.03 GPa of the target value. A vacuum distance of 12 Å was set to ensure sufficient vacuum and avoid interactions between two periods.

The van der Waals corrections to the total Kohn-Sham energy were incorporated into the calculations. The van der Waals corrections were applied using the DFT-D3 method[62]. The Mulliken charge and the potential energy distribution (PED) were calculated by vibrational energy distribution analysis (VEDA 4)[63].

Piezocatalytic property test

The eletrochemical property were measured using an electrochemical workstation (CHI 660E, Shanghai CH Instruments Co., Ltd.) under 1.5 W/cm² US irradiation. In addition, a three-electrode system was constructed in a quartz glass cell in 0.5 M Na_2SO_4 aqueous solution, using a Pt plate as the counter electrode, an Ag/AgCl electrode as the reference electrode and an experimental sample as the working electrode. Singlet oxygen ($^1O_2$) was detected by employing ESR (JES-FA200, Japan Electronics Co., Ltd) with 2,2,6,6-tetramethylpiperidine (TEMP, Aladdin) as the trapping agent.

In vitro antibacterial test

MRSA was purchased from American Type Culture Collection (ATCC, Manassas, VA). To explore the antimicrobial capacity of the material itself, 10^6 CFU/mL MRSA was used for evaluation. 10 μL of MRSA suspension was taken and diluted 200 times with each nanosheet and vancomycin solution (200 μg/mL). Then, the mixture was shaken at 37°C for 24 h, and 20 μL suspension is taken at 0, 4, 8, 16 and 24 h for spread plate experiments. The groups were: Control, Van, MON(Cu), MON(CuMn) and MON(CuMn)-Q.

In order to investigate the sonodynamic antibacterial ability of the material, 10^6 CFU/mL MRSA solution was used for spread plate experiments. Specifically, 10 μL of MRSA suspension was taken and diluted 200 times with each nanosheet solution (200 μg/mL). Additionally, 200 μg/mL vancomycin solution was used for comparison with the nanosheet solutions. The mixture in the US group and each nanosheet group was then treated for 15 minutes under US irradiation (1.0 MHZ, 1.5 W/cm², 50% duty cycle). Next, 20 μL of suspension was collected for spread plate experiments. Finally, the plates were placed in a incubator at 37 °C for 24 hours and then counted. The experimental groups were as follows: Control, US, Van, MON(Cu) + US, MON(CuMn) + US and MON(CuMn)-Q + US. To observe the morphology of the bacteria, the FE-SEM (S-4800, Hitachi) was applied.

Hemolysis test

1 mL of rat 5% erythrocytes (Shanghai Yuanye Biotechnology Co., LTD) was transferred to a 1.5 mL EP tube and subjected to centrifugation at $200 \times g$ for 15 minutes, after which the supernatant was removed. The erythrocytes were resuspended following three washes of the precipitate with saline. The MON(CuMn)-Q was added to the erythrocyte suspension in order to achieve final concentrations of 25 μg/mL, 50 μg/mL, 100 μg/mL, 150 μg/mL, 200 μg/mL, and 250 μg/mL. 20 μL of RIPA lysate (BL504A, Biosharp) was added to another tube of erythrocyte suspension, which served as the positive control. Another tube of erythrocyte suspension was prepared without any added material and served as the negative control. Given that the nanosheets exhibit a colour that could potentially influence the determination of the final absorbance, we have additionally configured the MON(CuMn)-Q solution with the corresponding concentration as the background. The EP tubes of each group were incubated at 37°C for 1 h and then centrifuged at $200 \times g$ for 15 minutes. Subsequently, 100 μL of the supernatant was taken and the absorbance at 540 nm was measured. The percentage of haemolysis was calculated using the following formula:

$$\text{Hemolysis(\%)} = (\text{OD}_{\text{Samples}} - \text{OD}_{\text{Background}})/ \\ (\text{OD}_{\text{Positive Control}} - \text{OD}_{\text{Negative Control}}) \times 100\% \quad (4)$$

Cell culture

hBMSCs were obtained from bone marrow blood of healthy volunteers. These volunteers were recruited from the department of orthopaedic surgery of Wuhan Union Medical College in compliance with the ethical committee of Tongji Medical College of Huazhong University of Science and Technology (HUST) (No. S347). Briefly, the steps are to mix bone marrow blood, lymphocyte separation solution and sterile PBS and then centrifuge to obtain hBMSCs. Immortalised HUVECs and THP1 were bought from the companies (Hunan Fenghui Biotechnology Co., Ltd, Shanghai Biyuntian Biological Co., Ltd.). The short tandem repeat (STR) technology was employed for cell identification. hBMSCs and HUVECs were cultured in DMEM/F12 medium (Boster Biological Technology Co., Ltd). THP1 was cultured in 1640 medium (Boster Biological Technology Co.,Ltd). The medium was also supplemented with 10% fetal bovine serum and 1% penicillin-streptomycin solution (Boster Biological Technology Co., Ltd) and all cells were cultured at 37 °C.

CCK8 assay

Firstly, A total of 1×10^4 cells per well were seeded in 24-well plates and co-cultured with different concentrations of nanosheets. Furthermore, after the set incubation period, the culture medium with or without nanosheets was removed with 10% CCK8 solution (AC11L054, Life-iLab) and incubated at 37 °C for 1 h. Finally, liquid (100 μL) from each well was transferred to 96-well plates, and the absorbance at 450 nm was recorded.

To investigate the impact of US on cell viability, 5×10^5 hBMSCs were seeded in six-well plates and co-cultured with 150 μg/mL MON(CuMn)-Q before the US. The parameter of US is: 1.0 MHZ, 1.5 W/cm², 50% duty cycle, 15 min. Cells before US and on day 1, day 3, day 7 and day 14 after US were subjected to CCK8 assay.

Quantitative real-time fluorescence polymerase chain reaction

HUVECs were seeded in 6-well plates and then incubated for three days under the different conditions. The groups were Control, MON(Cu), MON(CuMn) and MON(CuMn)-Q. After incubation, RNA was extracted using the FastPure® Cell/Tissue Total RNA Isolation Kit V2 (Vazyme Biotech Co., Ltd), and the procedure was carried out in accordance with the instructions. The extracted RNA was then quantified using an ultra-micro spectrophotometer (Applied Biosystems). To obtain complementary DNA (cDNA), HiScript III RT SuperMix (R323-01, Vazyme) was added to the RNA solution and the mixture was reverse transcribed into cDNA using a reverse transcription instrument (Applied Biosystems). Finally, the prepared cDNA, primer, SYBR fluorescent dye (Q712-02, Vazyme), and DEPC water (BL510A, Biosharp) were mixed and a real-time fluorescence quantitative PCR system (BioRad Laboratories) was applied to detect each target gene. The primer sequences were listed in Supplementary Table 5. The Cq values were normalised using GAPDH, and the expression was calculated according to the $2^{-\Delta\Delta CT}$ method. The reaction procedure involved a denaturation step at 95 °C for 30 seconds, followed by an annealing step at 95 °C for 5 seconds and an extension step at 55 °C for 10 seconds, repeated for 40 cycles.

Western blot

Total cellular proteins were collected by radio-immunoprecipitation assay (RIPA, BL504A, Biosharp) using a mixture of protease and phosphoproteinase inhibitors (BL615A and BL612A Biosharp). Protein samples were separated by sodium salt-polyacrylamide gel electrophoresis (SDS-PAGE) electrophoresis and transferred to the membrane. The membrane was then blocked with 0.1% Tris Buffered Saline Tween (TBST) blocking solution containing 5% bovine serum albumin (BSA, BS114, Biosharp) for 1 h. Primary antibodies were incubated overnight at 4°C and the membrane was washed three times with PBS.

The membrane was washed three times with 0.1% TBST and then incubated with the appropriate secondary antibodies at room temperature for 1 h. The membrane was then visualised, photographed and analyzed semiquantitatively on a chemiluminescence imaging system (Tanon 5200, Tanon). The information of antibody was presented in Supplementary Table 6.

Immunofluorescence
Cells were seeded in six-well plates, incubated for a period of time and then the medium was removed. The cells were then fixed with 4% paraformaldehyde for 30 minutes, followed by incubation with 0.5% Triton X-100 for 20 minutes at room temperature, rinsed three times with PBS, and then blocked with immunofluorescence blocking solution (P0102, Beyotime) for 30 minutes at room temperature, followed by the addition of a specific amount of primary antibody prepared with TBST and incubated overnight at 4 °C in a humidity box. The next day, the cell well plates were washed three times on a horizontal shaker. The cells were covered with primary antibody of the appropriate genus and incubated at room temperature for 60 min, washed with 0.1% Phosphate Buffer Saline Tween (PBST), then DAPI stain (C1002, Beyotime) was added to the slides and incubated at room temperature for 10 min, protected from light. Finally, the images were observed and captured under a fluorescence microscope. In addition, confocal (LSM900, Zeiss) was used to observe the polarization of macrophages.

Cytoskeleton tracking was conducted using the Tubulin-Tracker kit (C2215S, Beyotime). The procedure was as follows: the Tubulin-Tracker Deep Red staining working solution was initially configured, the cell culture was removed, the cells growing on the crawler slides were washed with PBS, and after addition of the working solution, the cells were incubated at 37 °C for 1 h. Finally, the cells were photographed using confocal microscopy.

Alizarin Red S staining
hBMSCs were cultured in for 21 days in culture medium containing 50 μg/mL MON(Cu), 100 μg/mL MON(CuMn) and 150 μg/mL MON(CuMn)-Q, respectively. hBMSCs cultured in medium without nanosheet for 21 days were set as the control group. Then cells were washed with PBS and fixed in 4% paraformaldehyde solution for 30 min before staining. Appropriate amount of 0.2% Alizarin Red S solution (G1450, Solarbio) was added, evenly cover the cells, and stain at room temperature for 30 min. Then the cells were washed with PBS thoroughly, and can then be viewed and photographed under a microscope.

Alkaline phosphatase staining
hBMSCs were cultured in for 14 days in culture medium containing 50 μg/mL MON(Cu), 100 μg/mL MON(CuMn) and 150 μg/mL MON(CuMn)-Q, respectively. hBMSCs cultured in medium without nanosheet for 14 days were set as the control group. Then cells were washed with PBS and fixed in 4% paraformaldehyde solution for 30 min before staining. Appropriate amount of ALP staining solution (C3206, Beyotime) was added, evenly cover the cells, and stain at room temperature for 30 min. Then the cells were washed with PBS thoroughly, and can then be viewed and photographed under a microscope.

RNA sequencing
The hBMSCs were divided into two groups: the Control and the MON(CuMn)-Q groups. The cells in the MON(CuMn)-Q group were cultured with 150 μg/mL of the nanosheet for 21 days. Cells in the control group were cultured for 21 days in a medium containing no material. Moreover, total RNA was extracted using TRIzol Reagent (15596026, Invitrogen). RNA samples were quantified after being tested the quality and integrity. Then an RNA sequencing library was built.

Raw sequencing data were analyzed with the assistance of QL Bio (Beijing, China) using Novaseq 6000 PE150 (Illumina, USA) with default parameters. GO analysis and KEGG enrichment analysis of differentially expressed genes were performed with a P-value cut-off of 0.05.

Cell flow cytometry
9×10^6 THP1 were seeded in T25 culture flasks and 50 ng/mL PMA was added to induce THP differentiation into macrophages for 3 days. To detect the immunomodulatory ability of the nanosheets, 1 ug/mL LPS and adherent THP1 were co-cultured for 2 days, followed by the addition of 1 mmol/L DMTU, 50 μg/mL MON(Cu), 100 μg/mL MON(CuMn) and 200 μg/mL MON(CuMn)-Q to the medium for 2 days. Macrophages were scraped from the culture flasks to detect macrophage polarisation, and a fixation/permeabilization kit (BD) was used prior to permeabilization to facilitate intracellular bicolor staining. The staining of CD86 and CD206 were achieved using fluorescein-labelled anti-mouse antibodies (BD) (Supplementary Table 6). Mitochondrial membrane potential and ROS staining were performed using the JC-1 staining kit and the ROS staining kit, respectively (S0033S, C2005, Beyotime).

While stimulating hBMSCs with 100 μmol/L H_2O_2, cells were co-cultured with 1 mmol/L DMTU, 50 μg/mL MON(Cu), 100 μg/mL MON(CuMn) and 150 μg/mL MON(CuMn)-Q for 3 days, respectively. The cells were then digested with pancreatic enzyme (C0201, Beyotime) and stained with JC-1 and ROS kits. After three times of PBS washing, the cells were detected by flow cytometry (FACSCalibur, BD Biosciences).

Tube formation experiment
5×10^5 HUVECs were seeded on six-well plates and cultured for three days by adding medium with or without nanosheets. The matrix gel (354230, Corning) should be placed in a refrigerator at 4°C overnight, one day prior to the experiment, in order for the gel to melt at a gradual pace. The cell culture medium should be removed and 300 μL of matrix gel was added to each well in a dropwise manner, with care taken to avoid the formation of air bubbles. The cells were then incubated for a period of 6 hours, after which they were photographed for observation.

Scratch assay
Firstly, a marker pen was used on the back of the six-well plate to draw even horizontal lines about every 0.5-1 cm across the hole. Cells in logarithmic growth phase were trypsinised into single cell suspension and seeded into six-well culture plates. The cell plate was 60,000 cells/well, and the inoculation principle was that the fusion rate reached 100% after overnight, and the final amount of medium per well was 2 ml. The cells were cultured at 37 °C in a 5% CO_2 incubator for 24 hours. Then, the plate was scratched parallel or perpendicular to the horizontal line behind the gun head with a 200-microlitre gun head. Then the cells were washed with PBS and the serum-free medium was added. Finally, the cross-line scratches with a marker behind the 6-well plate was erased and photos were taken at 0 and 6 time points.

Preparation and characterization of the hydrogel
In order to configure Je-1 hydrogel, Je-1 stock solution was first prepared at a concentration of 100 mg/mL of DMSO. Afterwards, the Je-1 stock solution was diluted to different concentrations using 1× PBS and incubated at 37°C for more than 15 min to form gels. To prepare MON(CuMn)-Q-J ointment, the Je-1 stock solution was diluted with a solution containing MON(CuMn)-Q to give a final concentration of MON(CuMn)-Q of 200 μg/mL. The vial tilt experiments were carried out to assess the formation of hydrogels. In addition, FE-SEM (S-4800, Hitachi) was used to observe the surface morphology of the gels.

Animal experiment

Spraque-Dawley (SD) Rats purchased from the laboratory animal centre of HUST were selected as the experimental animal model. All rats were male and weighed between 180 and 220 g. All experiments were approved by the animal research committee of HUST (No. S3946) and complied with international animal welfare standards. The SD rats were raised in accordance with standardised conditions of a specific pathogen-free environment, with a constant temperature of 21–24 °C and a 1:1 dark:light cycle. The animals were randomly and blindly assigned to groups for in vivo experiments. Rats were first anaesthetized with 3% pentobarbital (0.3 mg/kg) by intraperitoneal injection, and then the skin was prepared locally on the rat skull for surgery. The skin, subcutaneous tissue, muscle and periosteum were dissected with a scalpel from the bridge of the nose to the base of the skull to fully expose the parietal bone, and an 6 mm round full-thickness skull defect was created in the parietal bone using a 6 mm diameter trephine, which was flushed and cooled with physiological saline while maintaining the integrity of the dura mater. In the MRSA, the Van and the MON(CuMn) + US groups, 100 µL 10^8 CFU/mL of MRSA suspension was injected into the defects of rats. In the Control group, 100 µL of sterile saline was injected into the defects instead of the bacterial solution. After three days of surgery, the wounds in the MRSA-infected rats were reopened. 100 µL PBS or MON(CuMn)-Q-J was injected to the defects of the rats in the MRSA group and the MON(CuMn) + US group, respectively. 40 mg/kg vancomycin was injected into the tail vein of rats in the Van group. Then rats in the MON(CuMn) + US were treated by US. The US parameters were 1.0 MHZ, 1.5 W/cm² and 50% duty cycle, 1 MHz for 15 min. On the 14th day after treatment, SD rats were sacrificed for H&E staining and IF. Images around the wound were taken on the 14th day after treatment. Masson staining, H&E staining, IHC and IF were performed on the skulls of the rats after 28 days of treatment. The heart, liver, spleen and kidney were also collected for H&E staining. Renal function assessment was performed on on day 28 following the treatment.

To eliminate the potential confounding influence of Je-1's antimicrobial activity on the observed outcomes, we conducted an independent assessment of the therapeutic efficacy of Je-1 and MON(CuMn)-Q-J. Three days following the cranial injection of MRSA into the rats, the wounds were reopened and 100 µl of PBS, Je-1 and MON(CuMn)-Q-J were administered. A total of five rats that had been administered PBS were selected to receive additional US treatment, defined as the US group. Another five rats that had been administered PBS were selected to be the MRSA group. The rats that were administered Je-1 and MON(CuMn)-Q-J were subjected to US treatment, resulting in the formation of two distinct groups: the Je-1 + US group and the MON(CuMn)-Q-J + US group. On days 1, 3, and 7 following the administration of the treatment, tissues from the defects were collected for the purpose of spread plate experiment. Furthermore, tissues around defects were obtained on the initial day for Gram staining. A CT examination was conducted on the skull on day 28 post-treatment.

Acute toxicity test

Following the creation of a defect at the apex of the rat skull and the subsequent injection of MRSA, hydrogels comprising varying concentrations of MON(CuMn)-Q were employed to fill the aforementioned defect. Following a seven-day treatment period, the rats were sacrificed, and their serum was collected for subsequent analysis to assess liver and kidney function.

In order to ascertain the degree of skin irritation caused by the material, an intradermal irritation test was employed to determine the toxicity of the material[64,65]. The animal experiment has been approved by institutional animal care and use committee (IACUC) (No. 2024100902). nine female New Zealand rabbits, with a body weight exceeding 2 kg, were selected for the study. The rabbits were raised under a standard and specific pathogen-free environment with a constant temperature of 15–25 °C and a 1:1 dark:light cycle. The animals were randomly and blindly assigned to groups for in vivo experiments. Following a one-week period, during which the rabbits were fed, the hair on both sides of the spine on the back of each rabbit was removed 16 hours prior to the commencement of the test, to serve as test and observation sites. Ten points were selected on the left and right sides of the rabbit's back, with each point spaced at moderate intervals. The top five holes on the left were allocated to the sample group, the top five holes on the right were assigned to the 0.9% saline solution (polar negative control), the bottom five holes on the left were designated for the 5% SDS solution group (positive control), and the bottom five holes on the right were allocated to the sesame oil (non-polar negative control) group. The local and surrounding skin tissue reactions at the injection site, including erythema, oedema, and necrosis, were observed and photographed at 24, 48 and 72 hours following intradermal injection.

In vivo antibacterial test

To further evaluate the antibacterial capacity of MON(CuMn)-Q, 2 mm × 1 mm granulation tissues were collected from the defects for bacterial examination after 1, 3, and 7 days of the treatments. Subsequently, the samples were put into 10 ml of sterile PBS and homogenized for 5 min. Then 20 µL of the solution was used for spread plate experiments, and the plates were incubated for 24 h at 37 °C. Then viable bacterial counts were taken. After 1, 7, and 14 days of treatment, rats were sacrificed, and the skull was collected for Gram staining.

Routine blood test

The blood of rats was collected from the orbital vein on 14th day after treatment, and analyzed by an animal hematology analyzer (BC-2800vet, Mindray).

Micro-CT evaluation

The infected skull tissue was scanned by a micro-CT imaging system (skyscan1176, Bruker). Then CT-Vox software and SkyScan CT software were performed for 3D reconstruction and analysis,

Histological analysis

All samples except for the heart, liver, spleen, and kidney were decalcified for 21 days before slicing. The slices were then stained with H&E, Masson, and Gram staining. The slices were observed by an optical microscope.

Statistical analysis

The mean ± standard deviation was used to express our data. All experiments were performed at least three times. Two-tailed ANOVA and two-tailed unpaired Student's t test were used to assess the significant difference between group means. It was considered that $*p < 0.05$, $**p < 0.01$, $***p < 0.001$ and $****p < 0.0001$ were statistically significant, while $p > 0.05$ was considered non-significant (ns). The investigators were blinded to group allocation during data collection and analysis. No data or samples were excluded from the study.

Reporting summary

Further information on research design is available in the Nature Portfolio Reporting Summary linked to this article.

Data availability

The RNA-seq data generated in this study are available on the National Center for Biotechnology Information (NCBI) database under GSE279154 by visiting https://www.ncbi.nlm.nih.gov/geo/. Genes and corresponding primer sequences used for qRT-PCR are listed in Supplementary Table 5. Information on antibodies is provided in Supplementary Table 6. All data supporting the findings of this study are

available within the article and its supplementary files. Source data is available for Figs. 2c, f, 2h–l, 3a–d, 4a–g, 5a–c, 6c, 7b, c, f–i, k–m, 8e, f, 9b and Supplementary Figs. 3, 4b, 5a, 6–14, 17, 18, 19b, 20, 21b, 22, 23, 26, 27, 28b, 29b, 30b, 31b–c, 32–36, 37b, 40, 44b, 46, 47b, 48, 49, 51 in the associated source data file. Any additional requests for information can be directed to and will be fulfilled by the corresponding authors.Source data are provided with this paper.

References

1. Pearson, J. J. et al. In vivo hydroxyapatite scaffold performance in infected bone defects. *J. Biomed. Mater. Res. B Appl. Biomater.* **108**, 1157–1166 (2020).
2. Luo, Z. et al. Enhanced bacterial cuproptosis-like death via reversal of hypoxia microenvironment for biofilm infection treatment. *Adv. Sci.* **11**, e2308850 (2024).
3. Lei, C. et al. Heterostructured piezocatalytic nanoparticles with enhanced ultrasound response for efficient repair of infectious bone defects. *Acta Biomater.* **172**, 343–354 (2023).
4. Lei, J. et al. Sulfur-regulated defect engineering for enhanced ultrasonic piezocatalytic therapy of bacteria-infected bone defects. *Chem. Eng. J.* **435**, 14 (2022).
5. Feng, X. et al. Piezo-augmented sonosensitizer with strong ultrasound-propelling ability for efficient treatment of osteomyelitis. *ACS Nano* **16**, 2546–2557 (2022).
6. Widaa, A., Claro, T., Foster, T. J., O'Brien, F. J. & Kerrigan, S. W. Staphylococcus aureus protein A plays a critical role in mediating bone destruction and bone loss in osteomyelitis. *PLoS One* **7**, e40586 (2012).
7. Maldonado, R. F., Sá-Correia, I. & Valvano, M. A. Lipopolysaccharide modification in Gram-negative bacteria during chronic infection. *FEMS Microbiol. Rev.* **40**, 480–493 (2016).
8. Ma, L. et al. A Janus-ROS healing system promoting infectious bone regeneration via sono-epigenetic modulation. *Adv. Mater.* **36**, e2307846 (2024).
9. Feng, X. et al. Ultrasonic interfacial engineering of MoS(2) -modified Zn single-atom catalysts for efficient osteomyelitis sonodynamic ion therapy. *Small* **18**, e2105775 (2022).
10. Wang, H. et al. Ultrasound-controlled MXene-based Schottky heterojunction improves anti-infection and osteogenesis properties. *Theranostics* **13**, 1669–1683 (2023).
11. Geng, C. et al. Achieving clearance of drug-resistant bacterial infection and rapid cutaneous wound regeneration using an ROS-balancing-engineered heterojunction. *Adv. Mater.* **36**, e2310599 (2024).
12. Yuehua, Y. et al. Oxidative stress induces downregulation of TP53INP2 and suppresses osteogenic differentiation of BMSCs during osteoporosis through the autophagy degradation pathway. *Free Radic. Biol. Med.* **166**, 226–237 (2021).
13. Wang, J. C. et al. Ultrathin WOx nanoribbons with moderate ROS clearance and antibacterial abilities efficiently induce M2 macrophage polarization for diabetic bone defect repair. *Adv. Funct. Mater.* 11 (2023).
14. Wu, Z. et al. Manganese-based antioxidase-inspired biocatalysts with axial Mn-N(5) sites and 2D d-π-conjugated networks for rescuing stem cell fate. *Angew. Chem. Int. Ed. Engl.* **62**, e202302329 (2023).
15. Shang, L. et al. Ultrasound-augmented multienzyme-like nanozyme hydrogel spray for promoting diabetic wound healing. *ACS Nano* **17**, 15962–15977 (2023).
16. Li, G. et al. Fluorinated chitosan to enhance transmucosal delivery of sonosensitizer-conjugated catalase for sonodynamic bladder cancer treatment post-intravesical instillation. *ACS Nano* **14**, 1586–1599 (2020).
17. Xing, X. J. et al. Advances and perspectives in organic sonosensitizers for sonodynamic therapy. *Coord. Chem. Rev.* **445**, 25 (2021).
18. Zeng, W. W. et al. An ultrasound-excitable aggregation-induced emission dye for enhanced sonodynamic therapy of tumors. *Adv. Healthc. Mater.* **9**, 8 (2020).
19. Zhou, L. et al. Metal-polyphenol-network coated prussian blue nanoparticles for synergistic ferroptosis and apoptosis via triggered GPX4 inhibition and concurrent in situ bleomycin toxification. *Small* **17**, e2103919 (2021).
20. Meldrum, K. et al. Cerium dioxide nanoparticles exacerbate house dust mite induced type II airway inflammation. *Part Fibre Toxicol.* **15**, 24 (2018).
21. Liu, Y. et al. Effective antibacterial activity of degradable copper-doped phosphate-based glass nanozymes. *ACS Appl. Mater. Interfaces* **13**, 11631–11645 (2021).
22. Qi, W., Qi, W., Xiong, D. & Long, M. Quercetin: its antioxidant mechanism, antibacterial properties and potential application in prevention and control of toxipathy. *Molecules* **27**, 6545 (2022).
23. Peng, Z. et al. Integrated endotoxin-adsorption and anti-bacterial properties of platelet-membrane-coated copper silicate hollow microspheres for wound healing. *J. Nanobiotechnol.* **19**, 383 (2021).
24. Wan, Y. et al. Antibacterial zeolite imidazole frameworks with manganese doping for immunomodulation to accelerate infected wound healing. *Adv. Health Mater.* **10**, e2101515 (2021).
25. Li, Y. X. et al. 2D Zn-porphyrin-based Co(II)-MOF with 2-methylimidazole sitting axially on the paddle-wheel units: an efficient electrochemiluminescence bioassay for SARS-CoV-2. *Adv. Funct. Mater.* **32**, 2209743 (2022).
26. Li, J. et al. 2D MOF periodontitis photodynamic ion therapy. *J. Am. Chem. Soc.* **143**, 15427–15439 (2021).
27. Lei, J. et al. Sonodynamic amplification of cGAS-STING activation by cobalt-based nanoagonist against bone and metastatic tumor. *Biomaterials* **302**, 122295 (2023).
28. Liu, M. et al. Ultrathin metal-organic framework nanosheets as a gutter layer for flexible composite gas separation membranes. *ACS Nano* **12**, 11591–11599 (2018).
29. Wang, Y. et al. Bioinspired design of ultrathin 2D bimetallic metal-organic-framework nanosheets used as biomimetic enzymes. *Adv. Mater.* **28**, 4149–4155 (2016).
30. Zhao, Y. et al. Flexible polypropylene-supported ZIF-8 membranes for highly efficient propene/propane separation. *J. Am. Chem. Soc.* **142**, 20915–20919 (2020).
31. Xiang, K. et al. MOF-derived bimetallic nanozyme to catalyze ROS scavenging for protection of myocardial injury. *Theranostics* **13**, 2721–2733 (2023).
32. Kwon, K., Jung, J., Sahu, A. & Tae, G. Nanoreactor for cascade reaction between SOD and CAT and its tissue regeneration effect. *J. Control. Release* **344**, 160–172 (2022).
33. Yang, J., Yang, B. & Shi, J. A nanomedicine-enabled ion-exchange strategy for enhancing curcumin-based rheumatoid arthritis therapy. *Angew. Chem. Int. Ed. Engl.* **62**, e202310061 (2023).
34. Chen, Y. et al. Phenolic ligand-metal charge transfer induced copper nanozyme with reactive oxygen species-scavenging ability for chronic wound healing. *ACS Nano* **18**, 7024–7036 (2024).
35. Gravogl, L., Heinemann, F. W., Munz, D. & Meyer, K. An iron pincer complex in four oxidation states. *Inorg. Chem.* **59**, 5632–5645 (2020).
36. Wei, J. et al. Novel application of bergapten and quercetin with antibacterial, osteogenesis-potentiating, and anti-inflammation tri-effects. *Acta Biochim. Biophys. Sin.* **53**, 683–696 (2021).
37. Shen, L. & Ji, H. F. Theoretical study on physicochemical properties of curcumin. *Spectrochim. Acta A Mol. Biomol. Spectrosc.* **67**, 619–623 (2007).
38. Pullakhandam, R., Srinivas, P. N., Nair, M. K. & Reddy, G. B. Binding and stabilization of transthyretin by curcumin. *Arch. Biochem. Biophys.* **485**, 115–119 (2009).

39. Pastrana-Bonilla, E., Akoh, C. C., Sellappan, S. & Krewer, G. Phenolic content and antioxidant capacity of muscadine grapes. *J. Agric. Food Chem*. **51**, 5497–5503 (2003).

40. Marković, S. & Tošović, J. Application of time-dependent density functional and natural bond orbital theories to the UV-vis absorption spectra of some phenolic compounds. *J. Phys. Chem. A* **119**, 9352–9362 (2015).

41. Hassan, F. A., Ismail, A., Abdulhamid, A. & Azlan, A. Identification and quantification of phenolic compounds in bambangan (Mangifera pajang Kort.) peels and their free radical scavenging activity. *J. Agric. Food Chem*. **59**, 9102–9111 (2011).

42. Jomova, K. et al. Several lines of antioxidant defense against oxidative stress: antioxidant enzymes, nanomaterials with multiple enzyme-mimicking activities, and low-molecular-weight antioxidants. *Arch. Toxicol*. **98**, 1323–1367 (2024).

43. Choi, E. Y. et al. Relationship between the MIC of vancomycin and clinical outcome in patients with MRSA nosocomial pneumonia. *Intensive Care Med*. **37**, 639–647 (2011).

44. Diaz, R., Afreixo, V., Ramalheira, E., Rodrigues, C. & Gago, B. Evaluation of vancomycin MIC creep in methicillin-resistant Staphylococcus aureus infections-a systematic review and meta-analysis. *Clin. Microbiol. Infect*. **24**, 97–104 (2018).

45. Kunkalekar, R. K., Naik, M. M., Dubey, S. K. & Salker, A. V. Antibacterial activity of silver-doped manganese dioxide nanoparticles on multidrug-resistant bacteria. *J. Chem. Technol. Biotechnol*. **88**, 873–877 (2013).

46. He, Z. et al. Rejuvenating aged bone repair through multihierarchy reactive oxygen species-regulated hydrogel. *Adv. Mater*. **36**, e2306552 (2024).

47. Zhang, Q. et al. A factor-free hydrogel with ROS scavenging and responsive degradation for enhanced diabetic bone healing. *Small* **20**, e2306389 (2024).

48. Paul, S., Chhatar, S., Mishra, A. & Lal, G. Natural killer T cell activation increases iNOS(+)CD206(-) M1 macrophage and controls the growth of solid tumor. *J. Immunother. Cancer* **7**, 208 (2019).

49. Vander Heide, R. S., Sobotka, P. A. & Ganote, C. E. Effects of the free radical scavenger DMTU and mannitol on the oxygen paradox in perfused rat hearts. *J. Mol. Cell Cardiol*. **19**, 615–625 (1987).

50. Mahon, O. R. et al. Nano-particle mediated M2 macrophage polarization enhances bone formation and MSC osteogenesis in an IL-10 dependent manner. *Biomaterials* **239**, 119833 (2020).

51. Lin, Z. et al. Improved osteogenesis and angiogenesis of a novel copper ions doped calcium phosphate cement. *Mater. Sci. Eng. C. Mater. Biol. Appl* **114**, 111032 (2020).

52. Zhang, J. et al. Osteoimmunity-regulating biomimetically hierarchical scaffold for augmented bone regeneration. *Adv. Mater*. **34**, e2202044 (2022).

53. Das, A. et al. Cysteine oxidation of copper transporter CTR1 drives VEGFR2 signalling and angiogenesis. *Nat. Cell Biol*. **24**, 35–50 (2022).

54. Mu, G. et al. Calmodulin 2 facilitates angiogenesis and metastasis of gastric cancer via STAT3/HIF-1A/VEGF-A mediated macrophage polarization. *Front. Oncol*. **11**, 727306 (2021).

55. Zhang, H. et al. The antimicrobial, hemostatic, and anti-adhesion effects of a peptide hydrogel constructed by the all-d-enantiomer of antimicrobial peptide jelling-1. *Adv. Health Mater*. **12**, e2301612 (2023).

56. Zhou, J. et al. An injectable peptide hydrogel constructed of natural antimicrobial peptide J-1 and ADP shows anti-infection, hemostasis, and antiadhesion efficacy. *ACS Nano* **16**, 7636–7650 (2022).

57. Steinmetz, T., Eliakim-Raz, N., Goldberg, E., Leibovici, L. & Yahav, D. Association of vancomycin serum concentrations with efficacy in patients with MRSA infections: a systematic review and meta-analysis. *Clin. Microbiol. Infect*. **21**, 665–673 (2015).

58. Kresse, G. & Furthmüller, J. Efficiency of ab-initio total energy calculations for metals and semiconductors using a plane-wave basis set. *Comput. Mater. Sci*. **6**, 15–50 (1996).

59. Perdew, J. P., Burke, K. & Ernzerhof, M. Generalized gradient approximation made simple. *Phys. Rev. Lett*. **77**, 3865–3868 (1996).

60. Blöchl, P. E. Projector augmented-wave method. *Phys. Rev. B* **50**, 17953–17979 (1994).

61. Kresse, G. & Joubert, D. From ultrasoft pseudopotentials to the projector augmented-wave method. *Phys. Rev. B* **59**, 1758–1775 (1999).

62. Grimme, S., Antony, J., Ehrlich, S. & Krieg, H. A consistent and accurate ab initio parametrization of density functional dispersion correction (DFT-D) for the 94 elements H-Pu. *J. Chem. Phys*. **132**, 154104 (2010).

63. Ram Kumar, A. et al. Spectroscopic, biological, and topological insights on lemonol as a potential anticancer agent. *ACS Omega* **8**, 31548–31566 (2023).

64. Miyawaki, J., Yudasaka, M., Azami, T., Kubo, Y. & Iijima, S. Toxicity of single-walled carbon nanohorns. *ACS Nano* **2**, 213–226 (2008).

65. Taychaworaditsakul, W. et al. Safety of oral Carica papaya L. leaf 10% ethanolic extract for acute and chronic toxicity tests in sprague dawley rats. *Toxics* **12**, 198 (2024).

Acknowledgements

Author contributions

Z.X.O., J.Y.W., and J.L. conceived and designed the study. Z.X.O., J.Y.W., J.L., D.W., B.D.T., H.Z.L., H.C.W., X.Y.Z., D.C.Z., Z.D., and Y.F.D. performed the experiments and analyzed the data. H.P.X., L.T., X.B.F., and C.Y. supervised the project. Z.X.O. and J.Y.W. drafted the manuscript. All authors participated in interpreting the data and producing the final manuscript.

Competing interests

The authors declare no competing interests.

Additional information

Supplementary information The online version contains supplementary material available at https://doi.org/10.1038/s41467-024-54894-8.

Correspondence and requests for materials should be addressed to Lei Tan, Cao Yang or Xiaobo Feng.

Peer review information *Nature Communications* thanks Hongchang Lai and the other, anonymous, reviewers for their contribution to the peer review of this work. A peer review file is available.

Reprints and permissions information is available at http://www.nature.com/reprints

Publisher's note Springer Nature remains neutral with regard to jurisdictional claims in published maps and institutional affiliations.